JOM

A publication of The Minerals, Metals & Materials Society

ON THE ROAD TO GREEN: Vehicle Recycling in China

MARCH 2009

www.tms.org/jom.html

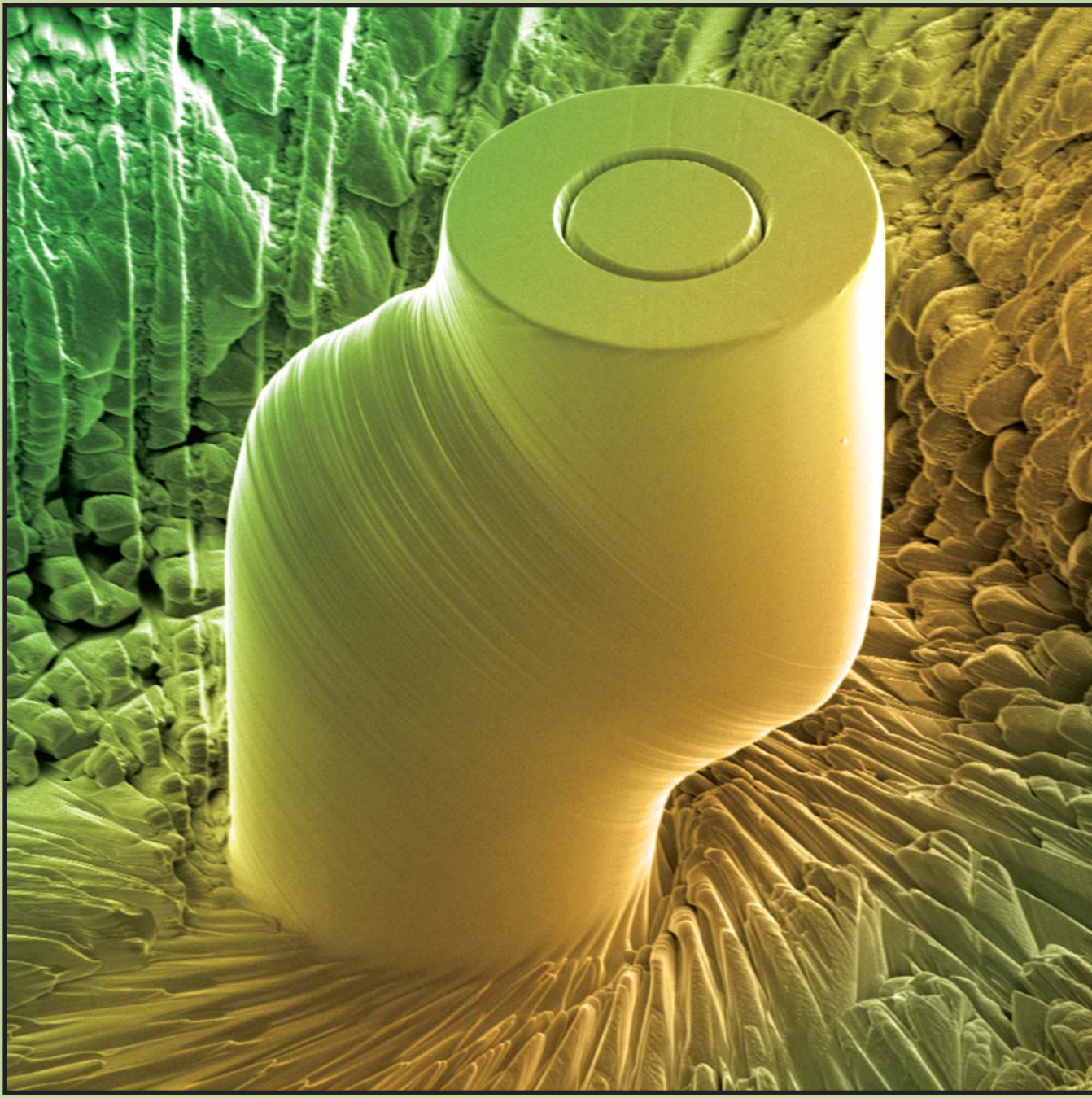

ADVANCED MATERIALS

- **Novel Techniques for Nanomechanical Characterization**

Revealing Deformation Mechanisms with Nanoindentation

D. Kiener, K. Durst, M. Rester, and A.M. Minor

For a better mechanistic understanding of the deformation phenomena that occur during nanoindentation testing, complimentary experimental techniques are critical. This overview presents several methods capable of analyzing the local microstructure of materials undergoing nanoindentation across different length scales, including etch pit analysis, electron backscatter diffraction, and in situ nanoindentation in a transmission electron microscope. Case studies of deformation mechanisms are provided, and the benefits and limitations of these complimentary experimental techniques are discussed.

INTRODUCTON

Measuring the hardness of a material is a simple principle dating back to Brinell.[1] A probe with a well-defined geometry, usually pyramidal, spherical, or conical, is placed on a testing sample and a load is applied. The hardness (H) of the material can then be defined as the load divided by the resulting projected area of the residual indent.[2] The simple and almost non-destructive measurement principle has led to the application of indentation techniques in various fields in material science, from brittle ceramics[3] to soft tissues.[4]

Significant advances in indentation techniques were made in the last 15 years based on instrumented indentation techniques, where the load is continuously measured as a function of the penetration depth.[5,6] Using the load versus displacement data and the unloading part of these curves, the contact stiffness can be measured and used for estimating the contact depth as well as the contact area between the tip and the sample.[7,8] It is regarded as advantageous to employ multiple partial unload segments or utilize a dynamic stiffness measurement technique to assess the stiffness during a single indent. However, it was shown recently that these testing procedures can result in lower measured hardness for various metals.[9,10] The quantitative analysis of such indentation data requires the determination of the tip shape (the so-called tip area function) and machine compliance.[11–13] With appropriate calibration, the modulus and hardness can be quantified at penetration depths as shallow as tens of nanometers.[5,14] For monolithic materials a depth-independent modulus is a good indication for a properly calibrated tip area function. Therefore, it is advantageous to plot these two quantities, hardness and modulus, as a function of the indentation depth[15,16] in order to ascertain the reliability of the hardness calculation. Observations of a depth-dependent elastic modulus in the case of a monolithic material may imply certain artifacts of the experiments, such as improper load-frame calibration, inaccurate tip area function, or surface roughness.

In the case of non-monolithic materials, where the modulus cannot be used to validate the tip area function, one approach to increase the accuracy of hardness measurements is to make direct measurement of the contact area. Optical microscopy or scanning electron microscopy (SEM) is useful, but cannot typically be used for sub-micrometer indentations. At this length scale, atomic-force microscopy (AFM) techniques are useful, and are available on many commercial indenter systems to locally image the sample surface before and after an indentation.[6] By this approach, nanoindents can be placed, for example, into the center of grains,[17] close to selected boundaries,[18] or on individual phases in the material.[19,20] Of course this limits the study to post-deformation characterization. For in situ observation of the de-

How would you…

…describe the overall significance of this paper?

This paper discusses experimental techniques for analyzing the local microstructure that results from deformation phenomena at small scales. Three characterization techniques are used to analyze nanoindentation-induced plasticity: etch-pit analysis, electron backscatter diffraction, and in situ TEM. No one technique describes the whole story, and multiple techniques are needed at different length scales to fully understand the deformation mechanisms that determine strength and ductility at small length scales.

…describe this work to a materials science and engineering professional with no experience in your technical specialty?

To understand the deformation phenomena that occur in a material during nanoindentation testing, complimentary experimental techniques are critical. This overview presents several methods capable of analyzing the local microstructure of materials undergoing nanoindentation across different length scales, including etch-pit analysis, electron backscatter diffraction, and in situ nanoindentation in a transmission electron microscope.

…describe this work to a layperson?

Measuring the hardness of a material is relatively easy—you simply press a sharp diamond indenter into the surface of a material, measure the force, and divide by the area of the resulting indentation. What is actually happening underneath the indenter is more difficult to assess. This paper describes methods of characterizing the deformation processes that occur at different length-scales underneath small indentations, that serve to better describe what determines the hardness of a material.

formation evolution during indentation, the indentation system may be placed in an SEM[21,22] or in a transmission electron microscope (TEM).[23]

While hardness H is the extractable plastic "property" from indentation experiments, it is usually of interest from a materials characterization perspective to assess the yield strength. To this end, there have been bulk estimations that link the hardness determined from indentation to the yield strength such as the Tabor rule[24] or the Marsh relation.[25] They work relatively well for indents that are large compared to the material microstructure. However, there is an inherent drawback to relating the bulk properties of a material to a nanoindentation test even in the case of monolithic materials: Plasticity in these small dimensions is a stochastic process,[26] governed by the discrete availability of features required to accommodate the prescribed deformation, for example individual dislocations, dislocation sources, or various kinds of boundaries. At very small scales the influence of the evolving deformation structure interacting with the surrounding microstructure is such that even the seemingly simple question of determining a material's yield point can become a subject for debate.

INDENTATION SIZE EFFECT

With ever decreasing indent size, different physical effects become important and the interaction of the indenter stress field with the local microstructure needs to be considered. This leads right to the question whether a material length scale exists that determines the material response. It is accepted that in the macroscopic polycrystalline bulk limit this length scale is set by the microstructure in terms of the smallest present obstacle blocking dislocations,[27] while at the micrometer scale usually the average dislocation spacing is regarded as the important length scale. But what if there is seemingly no length scale or microstructure involved? Even for single-crystalline materials, where these conditions are fulfilled, it was reported that the hardness is strongly dependent on the depth of indentation. Specifically, the hardness has been shown to decrease with increasing indentation depth, a feature termed the indentation size effect (ISE).[28–31] Various theories regarding the ISE have been discussed in the indentation literature.

The model of W.D. Nix and H. Gao,[31] predicting a scaling of the hardness with the inverse square root of the indentation depth, is perhaps the most widely cited, as well as the most widely debated. The model is based on strain gradient plasticity (SGP) theories,[32–35] and the concept is summarized in the following: Assume geometric self similarity of the indenter tip and the half-hemispherical plastic zone beneath the indent. Accommodation of the strain gradient caused by the indenter geometry is accomplished by geometrically necessary dislocations (GNDs).[36] The line length of these GNDs is proportional to h^2, where h is the indentation depth; the deformed volume is proportional to h^3. Thus, the GND density should be proportional to 1/h. The GNDs contribute to the local Taylor hardening and thus lead to higher hardness for smaller indents. From a fit of the indentation data to the Nix–Gao model a length scale can be extracted, which is expected to be characteristic for the material.[31,37] Combining Tabor's model on representative strain with the Nix–Gao approach, the hardness can be modeled from macroscopic stress versus strain curves to the depth-dependent hardness, even including the initiation of plasticity in the pop-in behavior.[38,39] While the Nix–Gao model can be applied to indentations, its physical basis is still under debate, and its validity cannot be addressed alone with load versus displacement characteristics.

Another rationale for the ISE is based on nucleation of dislocations. At very small indentation depths of several tens of nanometers, the material deforms initially elastically and sustains unusually high stresses until a critical stress is reached to nucleate defects required for the commencement of plasticity. Once this stress is reached, plastic deformation progresses in a discrete manner, leading to a staircase appearance in the load versus displacement behavior. Such incipient plasticity in indentation was studied by examination of the first pop-in events occurring during nanoindentation.[14,20,40–45] Describing this atomistic process by Hertzian contact mechanics,[46] contact pressures close to the theoretical shear strength of the material were evaluated before the pop-in event and related to dislocation nucleation events. Atomistic simulations of the indentation process of a perfect crystal[47–49] observed dislocation nucleation either heterogeneous from surface ledges or homogeneous below the indenter tip. The previously mentioned discrete and stochastic nature of plasticity in these small dimensions[26] is a distinct important feature, but neglected by the typical continuum-type analyses of hardness data. This may limit the applicability of such approaches.

It is clear that a deeper understanding of the mechanisms of plastic deformation during nanoindentation is essential for a more sophisticated mechanistic description, ranging from the macroscopic scale down to the nanometer scale. This demands the combination of nanoindentation techniques with other methods that are capable of locally analyzing the sample microstructure at the appropriate length scales. While this applies for any material, the focus of this article will be on crystalline materials, since most of the work in this area has been on crystalline metals or ceramics.

ETCH PIT METHODS

Understanding of deformation mechanisms of nanoindentation in crystalline materials requires the characterization of the associated dislocation structure. However, driven by the complex stress field underneath indentations, many slip systems can be activated in the plastic volume. This is associated with an inhomogeneous distribution of dislocations and locally high dislocation densities. Defining and measuring the dislocation density as a single scalar quantity is therefore an oversimplification of the problem. It is therefore of interest to consider both the distribution of slip together with the local dislocation density through spatially resolved measurements. To determine a local dislocation density can be difficult. A very convenient way to achieve this is through the etch pit method.

Ever since the work of Gilman and others, dislocation etch pit techniques on ionic crystals and later on metals have been used for fundamental studies of dislocation interactions.[50–52] During etching, dislocation lines exiting the surface are more strongly attacked than the defect-free bulk material in between. The dislocations are then imaged as etch

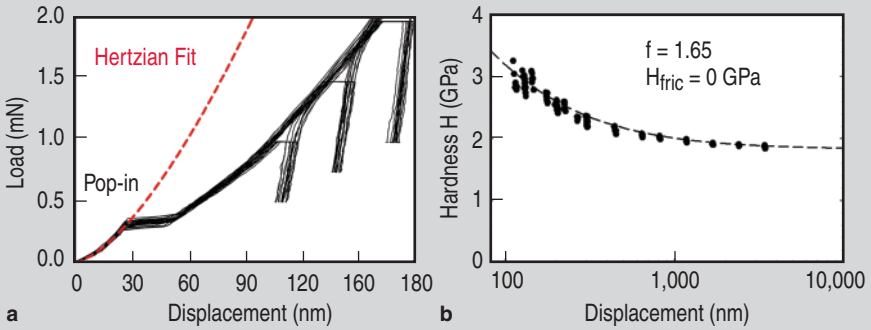

Figure 1. (a) Load versus displacement data for determining the depth-dependent hardness of CaF_2. A discrete well-defined transition from elastic to plastic deformation (pop-in) is found. (b) The depth-dependent hardness obtained from the load versus displacement data depicts a pronounced ISE. Figure adapted from Reference 58.

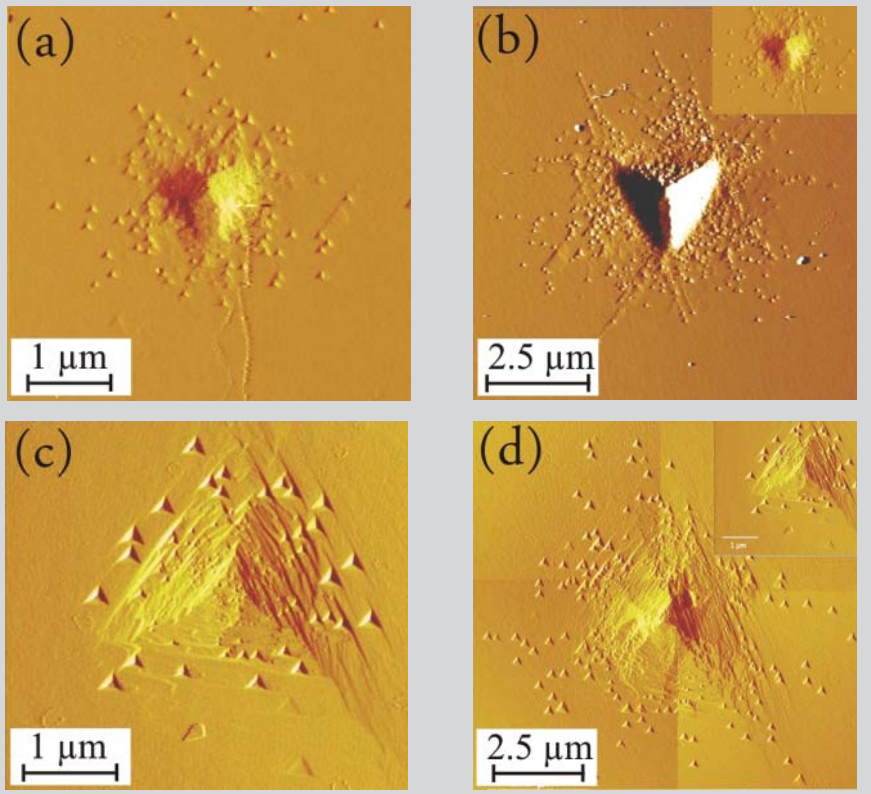

Figure 2. Atomic force microscopy deflection mode images showing dislocation structures around indentations into CaF_2. (a, c) Indentation with a peak load of 1 mN and a maximum penetration depth of 110 nm. (b, d) Indentation with a peak load of 5 mN and a corresponding maximum depth of 303 nm. Note that (a, b) were taken directly after indentation, while (c, d) depict the same indents after an additional polishing step. The inserts in (b, d) show the surface profiles for the 1 mN indentations with the same scaling as the 5 mN indentations for comparison reasons. Figure adapted from Reference 58.

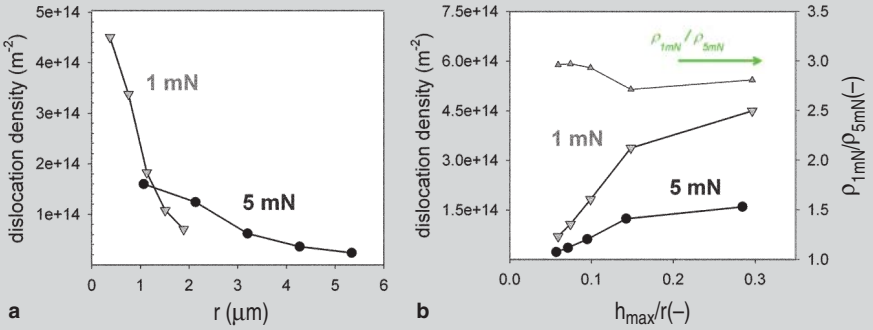

Figure 3. (a) The evaluated radial dislocation density for the two indents shown in Figure 2 for five different radii. (b) Radial dislocation density normalized by the maximum indentation depth h_{max}. Figure adapted from Reference 58.

pits in the surface, which additionally reveal the crystallographic symmetry. Ionic crystals are usually easily cleaved, allowing the preparation of a defined local crystallographic orientation with atomic level roughness. Therefore, the etch attack is well controlled and the dislocation structures are more easily revealed compared to metals. Etch pit techniques in conjunction with optical microscopy allow the determination of deformation structures like small-angle grain boundaries or individual dislocations in the grain interior.[53] Optical microscopy is limited in terms of lateral resolution, so SEM and other techniques can be used to study dislocation arrangements with small spacing. However, it has been shown that surface-sensitive techniques like AFM are well suited for revealing the etch pit structure. Minimum dislocation spacing in the order of 50 nm have been resolved by using the deflection mode signal for differentiation between overlapping etch pits,[54] yielding an upper limit to the detectable dislocation density of ~10^{13} cm^{-2}. Y. Gaillard et al.[55] revealed the dislocation structure around nanoindentation by sequential etching using etch pit techniques and AFM. For CaF_2, the etch pit rosette pattern around indentations has been studied previously.[56] However, no detailed analysis of dislocation densities and size effects is given in these contributions.

The etch pit technique can be easily applied to CaF_2, making it an interesting model material for testing the ISE. CaF_2 is an ionic crystal with the fluorite crystal structure. The lattice has a face-centered cubic (fcc) structure with three sub-lattices. CaF_2 cleaves on the {111} plane and slips on a {100} plane in <110> directions.[57] By cyclically changing the temperature by immersing the specimen in water baths, CaF_2 is cleaved along {111} planes. With this technique, a virtually deformation-free surface with atomic level roughness and mean dislocation spacing of ~60 µm is obtained. Thus, many artifacts that might affect the hardness measurement are circumvented. The presented measurements were achieved with little or no material preparation and serve as a good starting point for discussing the physical basis of the ISE.

The indentation tests were carried out using a calibrated Berkovich indenter tip

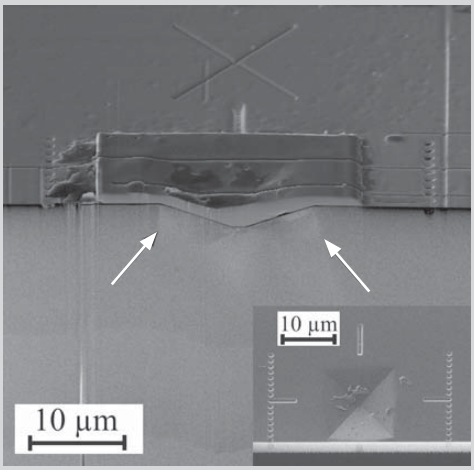

Figure 4. An inclined SEM view of a cross section through the center of a platinum covered Vickers indent. The local orientation changes beneath the indent can be deduced from the contrast variations and are indicated by arrows. The inset presents a top view of the uncovered indent and the surrounding markers. Data reproduced from Reference 63.

with the machine running in load control using a loading partial unloading profile for obtaining a high data density on hardness values. A detailed discussion on the experimental settings as well as the observed dislocation structure can be found in Reference 58. Figure 1 shows the basic experimental data on load versus displacement and the evaluated data on depth dependent hardness. The initial deformation seems to follow the Hertzian elastic contact and only after the so-called pop-in a residual permanent indentation depth can be found in the data. The first measures on hardness are obtained at indentation depths of around 100 nm and it is found that the hardness gradually decreases with increasing indentation depths. The hardness is plotted as a function of the displacement into the surface on a semi-logarithmic scale, so that the whole depth range is visible within one plot (Figure 1b). Using this data to extrapolate the macroscopic hardness H_0, the hardness as a function of indentation depth H(h) can be modeled with a modified Nix–Gao approach. An important factor there is the storage volume for GNDs, which is introduced via the factor f into the model. The fit (dotted line) gives a very good description of the measured hardness in the whole range of indentation depth from 100 nm to 3,500 nm.[58] From this data one clearly observes that the residual impression is formed initially by a pop-in and that only subsequently a depth dependent hardness is observed.

The important point to consider is the local distribution of dislocations. Therefore, the resulting etch pit structure of the indented crystals was imaged. It is assumed that these etch pits are directly related to the dislocation structure. Figure 2 shows AFM images of the indented CaF_2 surfaces in deflection mode contrast. Deflection mode images are particularly helpful when changes of the surface slope instead of the surface topography are of interest. Regions on the surface with small changes in topography are imaged with the same deflection mode signal, while edges or changing slopes of the surface are highlighted. This can be seen for example in Figure 2b, where the large black and white triangle represents the residual impression. With the change in surface slope at the middle of the indentation, the color of the image changes from black to white.

The small triangles adjacent to the large indentation are the dislocation etch pits, which reflect the symmetry of the indented {111} crystal plane. The sides of the etch pits represent <110> directions. Figure 2a and b depict the original surface after indentation. It is notable that the geometry of the indenter is clearly visible as a triangle. From the etch pit pattern the size of the plastic zone on the surface can be estimated. However, within the residual indentation no clear etch pit pattern is visible. This might be related to the fact that the indented contact area is highly deformed and moreover inclined with respect to the original {111} surface. The situation changes when removing an ~60 nm thick surface layer by polishing the crystal with SiO_2 suspension. The deformation zone is now clearly oriented along the <110> directions yielding a three-folded-symmetry (Figure 2c and d). Moreover, a clear dislocation structure with dislocation spacing well below the initial ~60 µm is now observable. The size of the etch pits depends on the dislocation density in its neighborhood. While the etch pits in the center of the indentation are quite small, large etch pits are observed at the outer areas of the plastic zone because for a low dislocation density the etching attack is localized at few dislocations. At higher densities, the etching attack is distributed over many dislocation lines, thus yielding smaller etch pits. In addition to the individual etch pits, a line

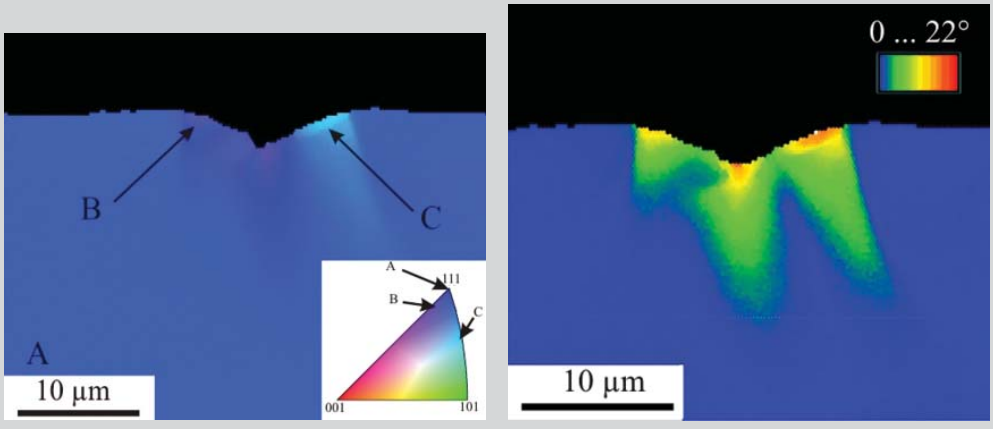

Figure 5. (a) An inverse pole figure (IPF) map and corresponding color code of the cross section shown in Figure 4. Three distinct areas are marked in the IPF map and the color code. (b) Orientation deviation (OD) map calculated from the same EBSD data. The color coding refers to the orientation deviation from the undeformed crystal. Data reproduced from Reference 63.

pattern becomes visible. Since no surface feature was visible before polishing, the line feature stems from the etching process. Presumably the lines are associated with the combined etching of the dislocation line and the inclined surface of the residual impression.

A quantification of the dislocation pattern was only possible after surface layer removal, since only then dislocations directly underneath the residual impression were clearly imaged. The dislocation density was quantified in radial coordinates around the center of the indentation using the coordinates of the individual dislocation etch pits. The radial dislocation density ρ(r) is given by two times the number of etch pits N in a given area with the radius of r, divided by this analyzed area: $\rho(r) = \frac{2N}{\pi r^2}$. The factor of two stems from stereographic considerations on analyzing a line length in a volume using the intersection points per area. The maximum radius is directly given by the observed extension of the plastic zone.

Figure 3 shows the radial dislocation density for the two different indentation depths at five discrete equidistant radii. The dislocation density at the maximum radius for each of the indentations is the total dislocation density found within the extension of the plastic zone. The dislocation densities clearly depend on the maximum load. At the lower load, where the displacement into the surface is three times lower compared to the higher load, the dislocation density is ~3 times higher. The two data sets indicate a dependence of the dislocation density on the analyzed area: The smaller the analyzed area the larger the dislocation density.

For better comparison of the two dislocation microstructures, the radial dislocation densities are normalized by the maximum indentation depth (Figure 3b). By doing so the two data sets are compared at the same depth-to-radius ratio. For a macroscopic indentation or in finite element simulations, this plot should yield the same stress distribution, regardless of the indentation depth.

Figure 3b is furthermore somewhat similar to the Nix–Gao plot,[31] where H^2 is plotted vs. 1/h. In the present case h_{max} is constant and r is varied along with the size of the plastic zone. For both loads, the dislocation density increases with 1/r, yielding larger densities at the center of the indent. Comparing the two densities to each other at the same h_{max}/r ratio, it is quite striking that $\rho_{1mN} / \rho_{5mN} \approx 3$, independent of the computed area. The dislocation density around the smaller indentation is thus larger than the dislocation density of the larger indentation, as predicted by the Nix–Gao model.[31]

The analyzed dislocation distribution underneath the indenter stems from several factors. On a macroscopic scale, the strain field around the indenter depends on the angle of the indenter and is self-similar with respect to depth. It is therefore expected that, on a macroscopic scale, the dislocation distribution around the indents should be self-similar and thus also scale with the indentation depth. At small scales, the material response depends also on the local strain gradient and therefore on the contact area or depth of indentation. The dislocation density around indentations at small scales is thus not directly comparable to large indentations. In general, modifications due to strain gradients will occur in the small scale case. Consequently, the difference in dislocation distribution around the two examined indentations is attributed to different strain gradients.

The next question is how the ratio of dislocation densities compares to the actual hardness measurements. Therefore, the hardness increase is compared to the increase in dislocation density. Without having any further information on the nature of these dislocations, both GNDs and statistically stored dislocations (SSDs) are imaged during this test. Since the relative size of the plastically deformed volume and all other factors affecting the hardness are the same for both indentation depths, only the dislocation density should influence the measured hardness. The ISE is quantified by using the hardness ratio and the ratio of the square root of the total dislocation density.[38,58] A hardness ratio $\frac{H_{1mN}}{H_{5mN}} = 1.34$ is found, the ratio of the root of dislocation densities yields

$$\frac{H_{Taylor}(1mN)}{H_{Taylor}(5mN)} \approx \frac{\sqrt{\rho_{1mN}}}{\sqrt{\rho_{5mN}}} = 1.7,$$

approximately independent of the analyzed volume. Both values point in the same direction, yielding a higher strength for the smaller indentation depth. Additional consideration of the frictional stress, which also accounts for the hardness of CaF_2, can resolve the discrepancy between measured hardness and the dislocation density based estimate on hardness.[58]

ELECTRON BACKSCATTER DIFFRACTION METHODS

While etch pit techniques are easily applied to surfaces, they cannot be easily extended to sub-surface characterization. Furthermore, without sectioning techniques, the etch pit methods are limited to the dislocations that penetrate the surface, while they are not sensitive to dislocations lying parallel to the surface or certain prismatic loops. To address the local crystal microstructure below nanoindentations, a few methods are available. Some TEM investigations use subsequent thinning steps of the sample backside to prepare plan view TEM specimens.[59–62] Unfortunately, the plan view geometry provides only the projection of the dislocation lines and leads in general to an area of high dislocation density in the center of the indent. This prevents further analysis of this heavily deformed zone.[61]

A more comprehensive understanding of the indentation process can be addressed by microstructural characterization of the indent in cross section. Therefore, a site specific preparation in conjunction with a characterization technique providing a high lateral resolution is needed. This can be accomplished by combining focused ion beam (FIB) milling for cross-section preparation with electron backscatter diffraction (EBSD) techniques to characterize the local microstructure beneath the sectioned nanoindentations.[15,16,63–65]

The preparation of indent cross sections with an FIB requires placing of the indents close to a sample edge in order to minimize milling time. First the sample surface is electrochemically polished, resulting in a better surface condition for subsequent indentation than mechanical polishing.[42,66] Second the perpendicular sample side is carefully polished using a 1 μm grained alumina suspension to form a sharp edge again. Using FIB, the width of the deformation layer introduced by

this mechanical preparation was determined to be ~5 μm for monolithic copper. The indentations were placed with sufficient distance to this deformed region. The experimental details concerning the indentation setup are given in References 16 and 63. A pronounced ISE was observed in all cases.[15,16,63] For example, the hardness of a {111} oriented copper single crystal decreased from 2.75 GPa at an indentation depth of 35 nm to ~0.6 GPa at a depth of ~250 μm.[65]

Before cross-sectioning the indent, the center is marked by thin FIB milled features to ease the subsequent site specific preparation. Subsequently, the top surface of the indent and its surrounding are covered by an approximately 500 nm thick tungsten or platinum protection layer for two purposes: First, it protects the surface region from the ion bombardment during sectioning.[67–69] Second, it allows EBSD analysis of the surface near region, since the strong background changes close to the edge would complicate the measurement. This is of particular importance for very shallow indents, where the first 100 nm of the protection layer are deposited by electron beam deposition instead of the commonly applied ion beam deposition. Focused ion beam milling starts with high milling currents (e.g., 2 nA) for high milling efficiency, while final steps utilize small currents (e.g., 100 pA) for a more precise geometry. An example of a cross section through the center of a Vickers indent is given in Figure 4. The inset shows the top view of the indent and the surrounding position markers before the protection layer was applied.[63]

Electron backscatter diffraction analysis was performed with a resolution of 20 nm. This sub-surface resolution is hard to achieve by conventional etching techniques. The result of an EBSD scan is the two-dimensional mapping of the local crystal orientation, given by three Euler angles.[70] For illustration in an inverse pole figure (IPF) map a color code is applied. While this is well suited to depict different grains or heavily deformed structures, the slight orientation differences occurring beneath an indent are hard to distinguish using this color coding. This can be seen in Figure 5a, which presents one IPF map to the relatively large indent shown in Figure 4. Therefore, orientation deviation (OD) maps are generated from the EBSD data, where for every data point the orientation deviation with respect to the undeformed crystal is plotted. This undeformed orientation can be determined by various techniques. However, using EBSD it is straightforward to measure it in a region with sufficient distance to the plastic zone of the indent, as long as the FIB polished region is large enough to encompass it. The OD map corresponding to the IPF map of Figure 5a is shown in Figure 5b. Here the plastically deformed zone can be distinguished more easily. However, plotting the data this way represents only the amount of crystal rotation; the directional information is lost. For example, from the IPF map shown in Figure 5a, or for higher accuracy from a pole figure plot of the area of interest,[16] it is seen that areas B and C are rotated in opposite directions with respect to the undeformed area A, (see also the arrows in the color code). This conclusion cannot be drawn from Figure 5b.

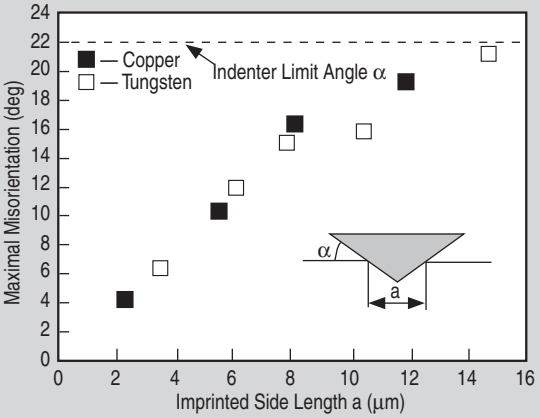

Figure 6. Maximum misorientation angle measured along the flanks of the indent for different sized Vickers indents into fcc copper (closed squares) and bcc tungsten (open squares). Data reproduced from Reference 63.

The experimental setup described can be applied to indentations with dimensions of several micrometers down to the sub-micrometer regime, which critically spans the bulk to discrete plasticity regimes. It is precisely across these length scales where the ISE is present and, more generally, where nanoindentation studies find their role in materials science. Clearly, the application of orientation measurements to nanoindentation-induced deformation structures will allow a more comprehensive understanding of the slip activity which governs the load versus displacement characteristics measured in nanoindentation. Moreover, this kind of analysis is not limited to cross sections through the indent center. Serial sectioning of the same indent was demonstrated elsewhere.[63] Furthermore, sectioning along selected glide planes of interest can also be accomplished. Thus, the full three-dimensional microstructure below nanoindentations can be determined.

Following the case study considered with etch pit techniques, the validity of the Nix–Gao model[31] can be investigated with the cross-sectional EBSD method. Two important assumptions of this concept can be analyzed with the EBSD technique. First, the model assumes a hemispherical plastic zone, and second, self-similarity of the evolving deformation structure is assumed.

From a qualitative view at the shape of the deformed zone depicted in Figure 5, it becomes clear that it deviates from the assumption of a half-sphere. There are reports of differently shaped deformation areas, depending on the indenter geometry.[16,63,64] This contradicts one of the basic assumptions of the Nix–Gao model, but can be corrected by using a correction factor that takes into account the actual dislocation storage volume.[38,39,71]

Regarding self-similarity, the strain gradient caused by the indenter as described by W.D. Nix and H. Gao[31] is given solely by the indenter geometry and is therefore constant for self-similar indenter shapes. An interesting difference between etch pit techniques and EBSD in this context is that the former is sensitive to all dislocations, while the latter detects only GNDs and is insensitive to SSDs. Thus, the misorientations observed by EBSD are caused by GNDs and are therefore directly related to strain gradients.[63]

Following the Nix–Gao model,[31] the observed misorientations, respectively strain gradients, should depend only on the indenter angle and not on the indent size. This was checked by investigating

the maximum misorientation observed along the indent flanks for different indent sizes. The results are shown in Figure 6 for Vickers indents into copper and tungsten. In contrast to the model, an increasing misorientation angle with increasing indent size is observed, which approaches the indenter limit angle for large indents. Transmission electron microscopy investigations of FIB prepared cross sections through Berkovich indents into (001) oriented copper single crystals confirmed these findings.[72]

Another interesting observation shown in Figure 6 is that the measured misorientations do not differ significantly between the fcc copper and the body-centered cubic (bcc) tungsten. Moreover, no significant influence of the crystal orientation or the crystal structure on the shape of the deformed zone was observed,[63] while surface investigations of slip lines around indentations depict differences for various crystal orientations.[73] The high stress beneath the indenter activates several slip systems, which causes a more or less orientation independent multi-slip deformation pattern. The situation changes near the free surface where the stress field diminishes. A further analysis on silver, copper, and nickel, all having an fcc crystal structure but different stacking fault energies of 16 $mJ \cdot m^{-2}$, 40 $mJ \cdot m^{-2}$, and 125 $mJ \cdot m^{-2}$, respectively, found no detectable influence of the stacking fault energy on the indentation-induced deformation patterns at room temperature.[15] The above results show the importance of cross-sectional investigations to support and extend the insights from surface investigations.

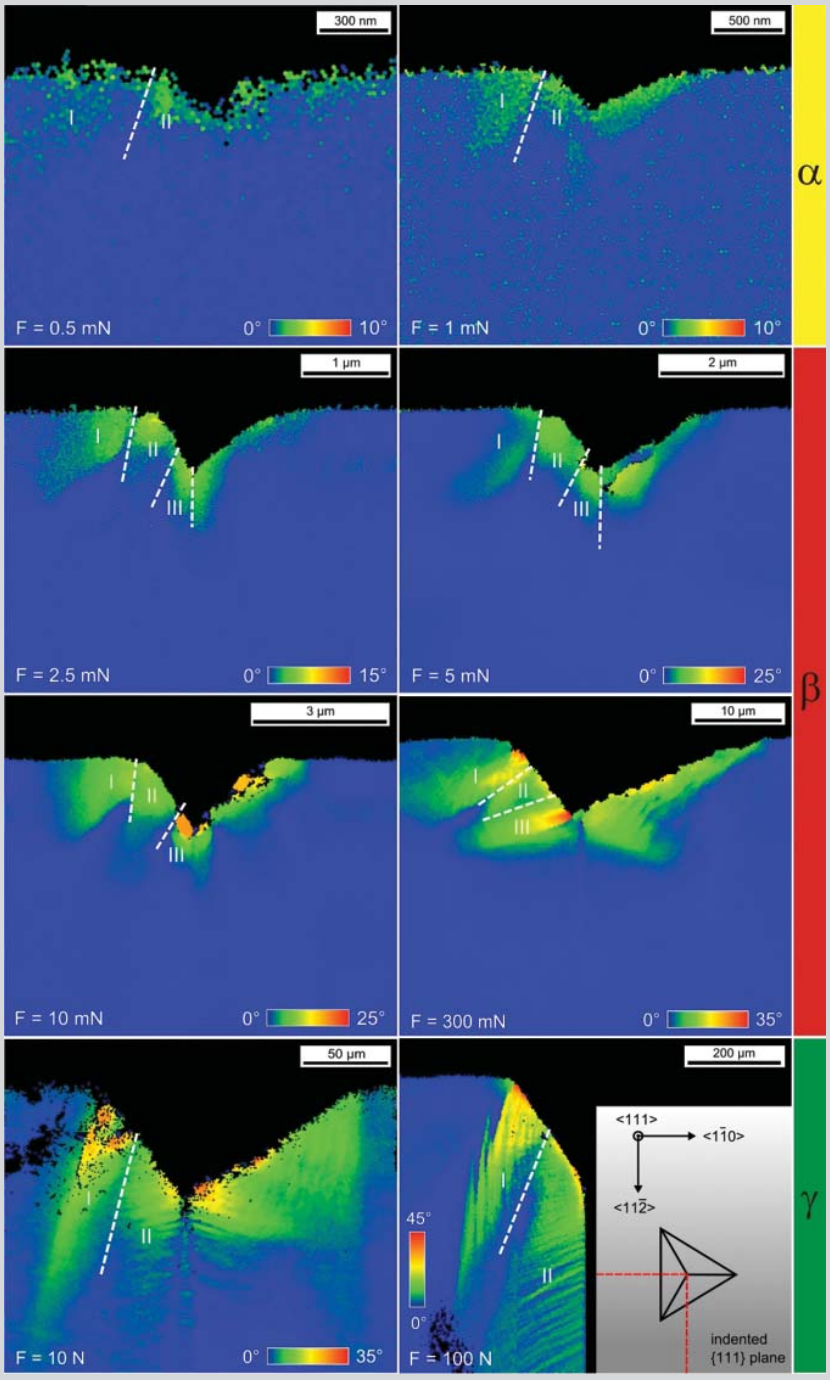

Figure 7. Size-dependent deformation patterns for the central cross section of cube corner indents (indicated in the schematic drawing) into monolithic copper with a (111) surface normal. On the left hand side of the indents, various deformation structures are observed. For small indents (α) only two regions with diffuse borders are present. In the intermediate size regime (β) three areas with clearly visible borders can be distinguished. For very large indents (γ) two regions with a fragmented microstructure are observed. Data reproduced from References 16 and 65.

A detailed analysis focused on the size-dependent formation of individual structures in the plastic zone to track down changes in the deformation structures forming during nanoindentation.[16,65] The results for central cross sections through cube corner indents in single-crystal copper with a (111) surface normal are depicted in Figure 7. Note that for the orientation deviation maps different color codes are applied. Again increasing maximum misorientations with increasing indentation size are observed. Focusing on the left-hand side of the indents, different deformation structures are observed for the investigated indent sizes. In the case of small indents (α) only two misoriented areas with diffuse borders appear. For intermediate indents (β) three clearly distinguishable regimes with differing orientation with respect to the undeformed material are indicated. Transmission electron microscopy investigations of these indents analyzed by EBSD were performed and confirmed the formation of small angle grain boundary-like dislocation arrangements and subgrains for indents in this size range.[74,75] The largest investigated indents (γ) depict two areas where severe deformation took place. Both regions show a fragmented substructure formation.

These different deformation structures

govern the hardness of the material in the different regimes. Correlating size-dependent hardness plots with the deformation structures, differing slopes of the plots were identified, in accordance with the observed changes of the deformation patterns.[16,22,65] While the Nix–Gao model[31] envisions a single, self-similar deformation mechanism, the observation of varying deformation regimes poses the question as to whether such a model is too simple.

The presented EBSD results and supporting TEM investigations,[74,75] suggest that deformation for the intermediate indents, and thus in the presence of a sufficient number of dislocation sources, is governed by pile-up of dislocations at the indenter flanks and in areas where the sign of the local shear stress field changes.[76] In the case of the largest indents, the observed fragmentation, as known for low and medium deformed single crystals,[77] leads to a substructure size that governs the hardness of the material. For shallow indents the limitation of dislocation sources requires far reaching dislocation loops to accommodate the deformation.[16]

IN SITU TRANSMISSION ELECTRON MICROSCOPY

While conventional instrumented nanoindentation tests are able to quantitatively measure the mechanical behavior of materials, the discrete deformation mechanisms that contribute to the measured behavior are rarely observed directly. Typically, the mode of deformation during a nanoindentation test is only studied ex post facto, or by indirect techniques such as in situ Raman spectroscopy[78] and in situ electrical resistivity measurements.[79] However, to truly observe the microstructural response of a material during indentation the deformation must be imaged at a resolution on the same order as the size of the defects created. A TEM can provide sub-nanometer resolution with the ability to image sub-surface phenomena such as the

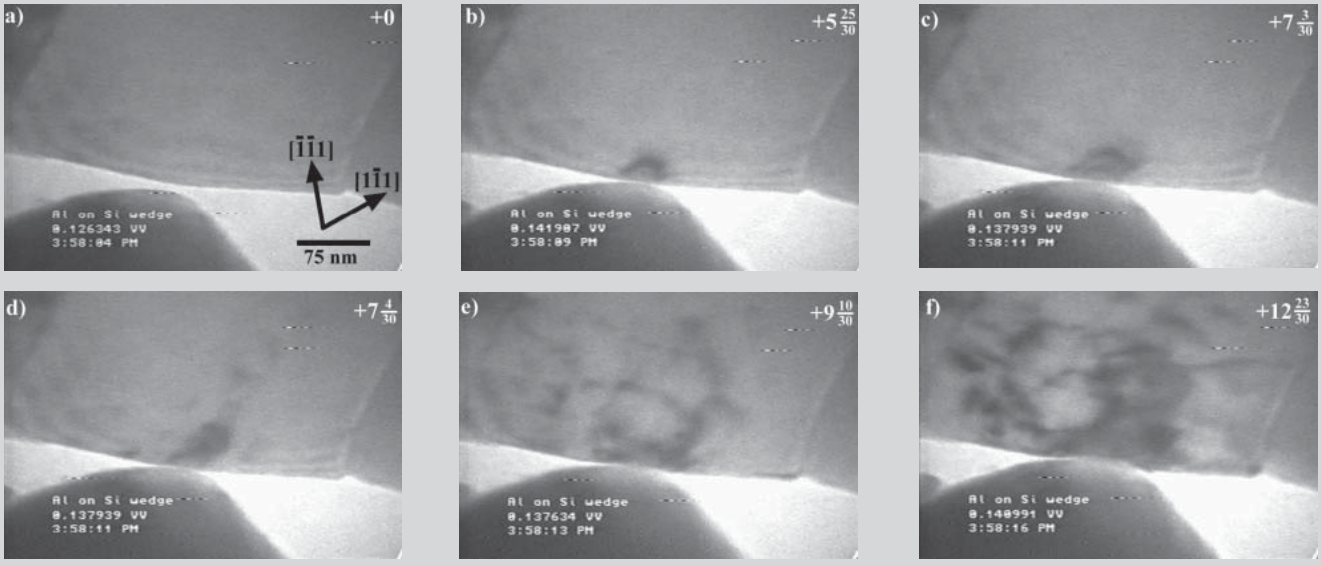

Figure 8. Time series TEM images of an aluminum grain showing the evolution of elastic-plastic deformation during an in situ nanoindentation experiment. The time elapsed from image (a) is given in seconds in the upper right corner of each frame. At (a) the grain is initially defect-free. At (b) the diamond indenter makes contact with the surface and elastic strain contours can be seen within the grain. Somewhere between images (c) and (d) dislocations are nucleated. (e) and (f) show the progression of dislocation plasticity as dislocations fill the grain. Figure taken from Reference 86.

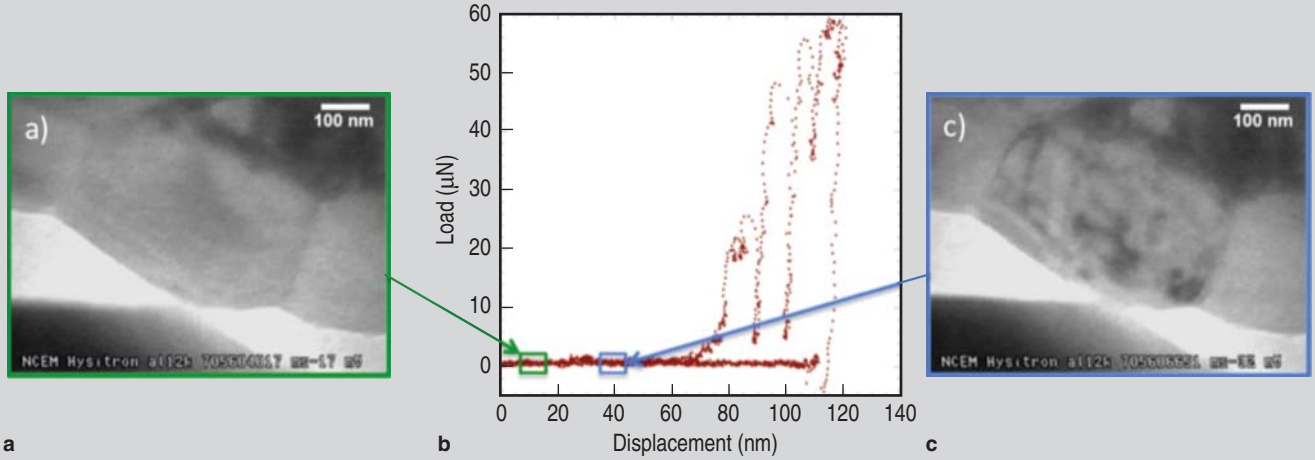

Figure 9. Quantitative in situ TEM nanoindentation of an initially dislocation-free submicrometer aluminum grain using a Berkovich conductive diamond indenter.[85] (a) The diamond indenter approaches the defect-free aluminum grain from the bottom of the video frame. (b) Displacement-controlled load versus displacement curve. (c) The microstructure change resulting from the first dislocation burst, occurring before sustained contact (denoted by the large increases in load that occur around 70 nm in displacement in (b)) is established. Figure adapted from Reference 85.

creation of dislocations and nucleation of phase transformations. However, the phenomenological interpretation of nanoindentation tests, and indeed the mechanical behavior of solids at their elastic limit, can be addressed by the experimental technique of in situ nanoindentation in a TEM. This experimental technique has shown direct observations of the nanoindentation-induced deformation behavior in bulk materials[80,81] and thin films.[23,82–85]

In order to perform a nanoindentation test inside a TEM, the sample must be oriented so that it can both be approached by the indenter tip and imaged with the electron beam. In addition, the sample thickness must be small enough to be electron transparent while also large enough to allow for indentation with a finite-sized tip. In most cases, sample thicknesses are on the order of 200–300 nm and a 75 nm radius of curvature is determined for the diamond tip (for further details see References 23, 80–85).

During an in situ nanoindentation test, video-rate images that are captured can be interpreted as quasi-static images of the equilibrium configuration of defects. Figure 8 illustrates this point by showing a series of six images taken from a video during an in situ nanoindentation experiment.[86] In Figure 8a, a diamond nanoindentation tip is approaching an aluminum grain that is ~400 nm in diameter. Figure 8b and c show images of the evolution of the induced strain contours during the initial stages of indentation, and correspond to purely elastic deformation in the absence of any preexisting dislocations that could cause plasticity. Figure 8d shows the first indication of plastic deformation, in which dislocations are nucleated; a set of prismatic loops is observed. Previous in situ nanoindentation studies on similar samples have also shown the nucleation of prismatic loops.[85] Figure 8c and d are consecutive frames of the video, and are 1/30th of a second apart. As can be seen, the exact location of the nucleation event is not discernable, since the evolution of the dislocation configuration has proceeded beyond the point at which that might be possible. Figure 8e and f shows the large increase in dislocation density achieved as deformation proceeds, and dislocations tangle and multiply.

Although the precise nucleation site may be difficult, if not impossible, to establish from such experiments, in situ indentation experiments provide unique advantages over ex situ TEM analysis of post-indent dislocation configurations. In addition to the difficulty in preparing TEM samples after indentations have been conducted, the strong image forces exerted on the dislocations by the free surface can lead to very different structures after the sample has been unloaded.

Furthermore, being able to directly correlate the microstructural evolution in a material with the quantitative force responses can lead to valuable insight for the interpretation of ex situ nanoindentation experiments. For instance, a recent quantitative in situ nanoindentation study of defect generation in aluminum thin films found that the initiation of dislocation plasticity can occur before sustained contact loading, at force levels that are barely discernable during instrumented nanoindentation.[85] In this study, the correlation of the in situ video and the load versus displacement curve showed that the initiation of defects occurred prior to the first sustained load drop that would normally be interpreted as the yield point in a displacement-controlled experiment (see Figure 9).[85] It was already noted that for in situ TEM studies such as this the available crystal volume is limited by the requirement of electron transparency. Fundamentally, this has the consequence that the analyzed volumes are smaller than what can be characterized by the other techniques described in this paper. For example, the volume imaged in Figure 9 is much smaller than what would be represented by the Nix–Gao model, and in fact the extent of the dislocation arrangement is controlled by the microstructure of the thin film (blocked by the grain boundaries) as opposed to any fundamental length scale that might be seen in a single crystal. Thus, more widespread dislocation arrangements need to be characterized by other techniques such as etch pit analysis,[58] EBSD investigations,[16] and post ex situ TEM examinations.[75]

Nevertheless, the experimental technique of in situ nanoindentation in a TEM has been shown to provide a unique capability for investigating the nanomechanical behavior of small solid volumes. Through quantitative in situ testing, a direct correlation is made between the microstructural evolution in a material and the load versus displacement signal generated by the indentation system. This capability is essential to fully understand the mechanisms associated with indentation phenomena and the fundamental deformation behavior of materials.

CONCLUSIONS

The presented techniques provide a wide range of additional information regarding the local microstructure of the indented volume, which is not accessible solely from the analysis of the load versus displacement data from nanoindentation experiments.

Etch pit methods depict the local arrangement of GNDs and SSDs in the plastic zone. This allows for the quantification of strain gradients and local fluctuations of the dislocation density with respect to indent size, indenter geometry and crystal orientation. Similar issues can be addressed by EBSD investigations, but this technique senses only GNDs and the orientation changes associated. The deduced orientation gradients are therefore equivalent to strain gradients,[63] since they are caused by the presence of GNDs. In the presented cases, the commonly harder accessible indent cross sections were investigated to complement the information from the surface etch pit results. There are differences between the two presented case studies, caused by the different indenters as well as friction stresses associated with different materials. At the same indentation depth, a Berkovich tip samples a much larger volume compared to a cube corner. Furthermore, the friction stress for CaF_2 is very high and leads to a confined plastic zone, while it is very low for copper, thus allowing the dislocations to move far into the underlying material. Nevertheless, the data gained with these techniques are essential to proceed from simple isotropic continuum models of the indentation process to more sophisticated descriptions taking into account the crystal anisotropy and size-dependent spatially varying strain gradients.

In situ nanoindentation in the TEM finally offers direct quantitative insight into incipient plasticity, since dislocation nucleation sites and nucleation stresses

can be deduced with high local resolution. The results shown indicate that the initially defect-free grain is filled with dislocations at marginal loads,[85] and that what is commonly regarded as the loading of a pristine single crystal appears to be more accurately described as indenting a crystal containing a high dislocation density.

The presented approaches all provide valuable insights, but differ in the investigated material and experimental parameters. Combination of all three approaches for a systematic study of a selected material system, using identical experimental parameters, might be a challenging but very promising goal. While etch pit methods and EBSD techniques would cover the three-dimensional microstructural evolution over a wide range of indentation sizes, in situ TEM nanoindentation would focus on initiation and temporal evolution of incipient plasticity. A study such as this would provide a unique assembly of information for complete analysis of the indentation process.

ACKNOWLEDGEMENTS

D.K. was supported by the Materials Center Leoben (MCL) within the Austrian Kplus Competence Center Programme. Financial support of K.D. by DFG (Deutsche Forschungsgemeinschaft) under contract Du 424-1/2 is gratefully acknowledged. M.R. acknowledges financial support by the FWF (Fonds zur Förderung der wissenschaftlichen Forschung) through Project P 17375-N07. A.M.M. was supported by the Scientific User Facilities Division of the Office of Basic Energy Sciences, U.S. Department of Energy under Contract # DE-AC02-05CH11231. The authors would like to thank all of their collaborators past and present who contributed to the results presented in this article.

References

1. J.A. Brinell, "Mémoire Sur les Épreuves à Bille en Acier," *Congrès International des Méthodes d'Essai des Matériaux de Construction,* vol. 2 (Paris: Vve Ch. Dunod , 1901), p. 83.
2. B.W. Mott, *Micro-indentation Hardness Testing* (London: Butterworths Publications Ltd., 1956).
3. S. Ndlovu, K. Durst, and M. Göken, *Wear,* 263 (2007), p. 1602.
4. O. Franke et al., *Acta Biomaterialia,* 3 (2007), p. 873.
5. W.C. Oliver and G.M. Pharr, *J. Mater. Res.,* 7 (1992), p. 1564.
6. A.C. Fischer-Cripps, *Nanoindentation* (New York: Springer, 2004).
7. G.M. Pharr, W.C. Oliver, and F.R. Brotzen, *J. Mater. Res.,* 7 (1992), p. 613.
8. I.N. Sneddon, *Int. J. Eng. Sci.,* 3 (1965), p. 47.
9. K. Durst et al., *Acta Mater.,* 55 (2007), p. 6825.
10. M.J. Cordill, N.R. Moody, and W.W. Gerberich, *J. Mater. Res.,* 23 (2008), p. 1604.
11. K.W. McElhaney, J.J. Vlassak, and W.D. Nix, *J. Mater. Res.,* 13 (1998), p. 1300.
12. A. Bolshakov and G.M. Pharr, *J. Mater. Res.,* 13 (1998), p. 1049.
13. J.G. Swadener and G.M. Pharr, *Phil. Mag. A,* 81 (2001), p. 447.
14. W.W. Gerberich et al., *Acta Met. Mater.,* 43 (1995), p. 1569.
15. M. Rester, C. Motz, and R. Pippan, *Scripta Mater.* 58 (2008), p.187.
16. M. Rester, C. Motz, and R. Pippan, *Acta Mater.,* 55 (2007), p. 6427.
17. B. Yang and H. Vehoff, *Acta Mater.,* 55 (2007), p. 849.
18. M. Rester, C. Motz, and R. Pippan, *J. Mater. Res.* (in press).
19. K. Durst and M. Göken, *Mater. Sci. Eng. A,* 387-389 (2004), p. 312.
20. M.J. Cordill et al., *Acta Mater.,* 54 (2006), p. 4515.
21. R. Rabe et al., Thin Solid Films, 469-470 (2004), p. 206.
22. D. Kiener et al., *Int. J. Mat. Res.,* 98 (2007), p. 1047.
23. A.M. Minor, J.W. Morris, and E.A. Stach, *App. Phys. Lett.,* 79 (2001), p. 1625.
24. D. Tabor, *Sheet Met. Ind.,* 31 (1954), p. 749.
25. D.M. Marsh, *Proc. R. Soc. Lond. A,* 279 (1964), p. 420.
26. F.F. Csikor et al., *Science,* 318 (2007), p. 251.
27. E. Arzt, *Acta Mater.,* 46 (1998), p. 5611.
28. N.A. Stelmashenko et al., *Acta Met. Mater.,* 41 (1993), p. 2855.
29. W.J. Poole, M.F. Ashby, and N.A. Fleck, *Scripta Mater.,* 34 (1996), p. 559.
30. Q. Ma and D.R. Clarke, *J. Mater. Res.,* 10 (1995), p. 853.
31. W.D. Nix and H. Gao, *J. Mech. Phys. Solids,* 46 (1998), p. 411.
32. N.A. Fleck et al., *Acta Met. Mater.,* 42 (1994), p. 475.
33. H. Gao et al., *J. Mech. Phys. Solids,* 47 (1999), p. 1239.
34. Y. Huang et al., *J. Mech. Phys. Solids,* 48 (2000), p. 99.
35. H. Mughrabi, *Mater. Sci. Eng. A,* 387-389 (2004), p. 209.
36. M.F. Ashby, *Phil. Mag. A,* 21 (1970), p. 399.
37. J.G. Swadener, E.P. George, and G.M. Pharr, *J. Mech. Phys. Solids,* 50 (2002), p. 681.
38. K. Durst et al., *Acta Mater.,* 54 (2006), p. 2547.
39. K. Durst, M. Göken, and G.M. Pharr, *J. Phys. D,* 41 (2008), p. 1.
40. N. Gane and F.P. Bowden, *J. App. Phys.,* 39 (1968), p. 1432.
41. T.F. Page, W.C. Oliver, and C.J. McHargue, *J. Mater. Res.,* 7 (1992), p. 450.
42. W.W. Gerberich et al., *Acta Mater.,* 47 (1999), p. 4115.
43. C.A. Schuh, J.K. Mason, and A.C. Lund, *Nature,* 4 (2005), 617.
44. E.T. Lilleodden and W.D. Nix, *Acta Mater.,* 54 (2006), p. 1583.
45. S. Vadalakonda et al., *Mater. Sci. Eng. A* 426 (2006), p. 208.
46. K.L. Johnson, *Contact Mechanics* (Cambridge, U.K.: Cambridge University Press, 1987).
47. A. Gouldstone, K.J. Van Vliet, and S. Suresh, *Nature,* 411 (2001), p. 656.
48. J. Li et al., *Nature,* 418 (2002), p. 307.
49. E.T. Lilleodden et al., *J. Mech. Phys. Solids,* 51 (2003), p. 901.
50. J.J. Gilman, W.G. Johnston, and G.W. Sears, *J. App. Phys.,* 29 (1958), p. 747.
51. W.G. Johnston and J.J. Gilman, *J. App. Phys.,* 30 (1959), p. 129.
52. V.R. Parameswaran, J. Weertman, and N. Urabe, *J. App. Phys.,* 43 (1972), p. 2982.
53. J.D. Livingston, *J. App. Phys.,* 31 (1960), p. 1071.
54. P. Sadrabadi et al., *Phil. Mag. Lett.* (submitted).
55. Y. Gaillard, C. Tromas, and J. Woirgard, *Acta Mater.,* 54 (2006), p. 1409.
56. O. Shikimaka and D. Grabco, *J. Phys. D,* 41 (2008), p. 074012.
57. A. Munoz, A. Dominguezrodriguez, and J. Castaing, *J. Mater. Sci.,* 29 (1994), p. 6207.
58. P. Sadrabadi, K. Durst, and M. Göken, *Acta Mater.* 57 (2009), p.1281.
59. W. Zielinski, H. Huang, and W.W. Gerberich, *J. Mater. Res.,* 8 (1993), p. 1300.
60. W. Zielinski et al., *Phil. Mag. A,* 72 (1995), p. 1221.
61. Y.L. Chiu and A.H.W. Ngan, *Acta Mater.,* 50 (2002), p. 2677.
62. D.E. Kramer et al., *Scripta Mater.,* 50 (2004), p. 745.
63. D. Kiener et al., *Acta Mater.,* 54 (2006), p. 2801.
64. N. Zaafarani et al., *Acta Mater.,* 54 (2006), p. 1863.
65. M. Rester, C. Motz, and R. Pippan, *Scripta Mater.,* 59 (2008), p. 742.
66. Y. Liu and A.H.W. Ngan, *Scripta Mater.,* 44 (2001), p. 237.
67. L.A. Giannuzzi and F.A. Stevie, *Introduction to Focused Ion Beams* (New York: Springer, 2005).
68. C.A. Volkert and A.M. Minor, *MRS Bull.,* 32 (2007), p. 389.
69. T.L. Matteson et al., *J. Electron. Mat.,* 31 (2002), p. 33.
70. V. Randle and O. Engler, *Introduction to Texture Analysis: Macrotexture, Microtexture and Orientation Mapping* (Amsterdam: Gordon & Breach, 2000).
71. K. Durst, B. Backes, and M. Göken, *Scripta Mater.,* 52 (2005), p. 1093.
72. K.K. McLaughlin and W.J. Clegg, *J. Phys. D,* 41 (2008), p. 1.
73. K.A. Nibur and D.F. Bahr, *Scripta Mater.,* 49 (2003), p. 1055.
74. M. Rester, C. Motz, and R. Pippan, *Mat. Res. Soc. Symp. Proc.,* 1049 (2007), p. AA003.
75. M. Rester, C. Motz, and R. Pippan, *Phil. Mag. Lett. 88* (2008), p. 879.
76. H.G.M. Kreuzer and R. Pippan, *Acta Mater.,* 55 (2007), p. 3229.
77. F. Schulz and H. Hanemann, *Z. Metallkd.,* 33 (1941), p. 124.
78. V. Domnich, Y. Gogotsi, and S. Dub, *App. Phys. Lett.,* 76 (2000), p. 2214.
79. J.E. Bradby, J.S. Williams, and M.V. Swain, *Phys. Rev. B* (2003), p. 67.
80. A.M. Minor et al, *Phil. Mag.,* 85 (2005), p. 323.
81. T. Ohmura et al., *J. Mater. Res.,* 19 (2004), p. 3626.
82. M. Jin et al., *Acta Mater.,* 52 (2004), p. 5381.
83. A.M. Minor et al., *J. Electron. Mat.,* 32 (2003), p. 1023.
84. A.M. Minor et al., *J. Mater. Res.,* 19 (2004), p. 176.
85. A.M. Minor et al., *Nature Materials,* 5 (2006), p. 697.
86. A.M. Minor et al., *J. Electron. Mat.,* 31 (2002), p. 958.

D. Kiener and M. Rester are with Erich Schmid Institute of Materials Science, Austrian Academy of Sciences, Leoben, Austria and the Department Materials Physics, Montanuniversität Leoben, Leoben, Austria; K. Durst is with Lehrstuhl 1–Allgemeine Werkstoffeigenschaften, Friedrich-Alexander-Universität Erlangen-Nürnberg, Erlangen, Germany; A.M. Minor is an assistant professor with the Department of Materials Science and Engineering, University of California, and the National Center for Electron Microscopy, Lawrence Berkeley National Laboratory, Berkeley, California. Dr. Kiener is also with the Department of Chemistry and Biochemistry, Ludwig-Maximilians-University Munich, Butenandtstr. 5-13 (E), 81377 Munich, Germany; 49-89-2180-77-569; fax 49-89-2180-77-622; e-mail daniel.kiener@cup.uni-muenchen.de.

Micro- and Nanoscale Tensile Testing of Materials

D.S. Gianola and C. Eberl

Enhanced for the Web

*This article appears on the JOM web site **(www.tms.org/jom.html)** in html format and includes links to additional on-line resources.*

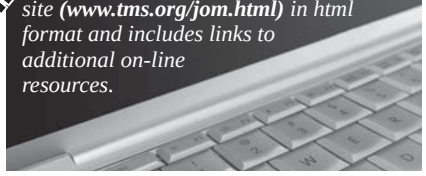

This article reviews concepts and techniques for performing instrumented tensile testing of materials at small dimensions. State-of-the-art methods to probe tensile behavior of micro- and nanoscaled materials span many orders of magnitudes of force and displacement, often requiring a custom solution for each new material discovery. We discuss the experimental opportunities, challenges, and pitfalls in concert with the scientific insights revealed from tensile investigations at length scales where conventional wisdom is challenged on how materials deform.

INTRODUCTION

Developing mechanical tensile testing techniques and methodologies of materials in miniscule dimensions to accompany the accelerating pace of technological miniaturization has been a challenging task. Novel device architectures have been proposed that utilize tiny building blocks (e.g., hybrid materials, nanocomposites, microelectromechanical systems [MEMS] and nanoelectromechanical systems [NEMS] materials, nanostructured thin films, nanoporous structures, nanowires, and nanotubes) because of their superior properties, even in the absence of a complete understanding of the governing mechanisms for deformation. The race is on to uncover the mechanisms that give rise to different properties when atomic scales are approached and change our thinking on how materials deform. Yet, the accurate and reliable testing at these length scales is shrouded with uncertainty.

The following experimental questions arise: How can we fabricate small specimens with good geometric tolerances? How do we measure the dimensions of small samples that cannot be imaged with conventional optical methods? How can we measure and apply small forces with high dynamic range? How do we manipulate and grip small specimens?

This article focuses on instrumented small-scale tensile (i.e., stretching or pulling) testing approaches, where load is applied uniaxially and the resulting stress and strain state is nominally uniform in the specimen. Simply stated, micro- and nanotensile approaches differ in comparison to other small-scale methods in that the interpretation of data is relatively straightforward, while the technical hurdles can be high. Conversely, techniques such as nanoindentation are relatively simple to execute, while the interpretation can be challenging.

How would you…

…describe the overall significance of this paper?

In this paper we review state-of-the-art small-scale tensile testing techniques spanning several orders of magnitude of size and highlight exemplary case studies that have a significant impact on various subjects in materials science.

…describe this work to a materials science and engineering professional with no experience in your technical specialty?

As technology miniaturizes, we need new techniques to probe the mechanical response of materials at pertinent length scales. Some methods we can simply scale down in size, but at increasingly small scales when test specimens have dimensions smaller than the diameter of a human hair (~50 μm), we need radically new approaches. Here we review tensile techniques at the micro- and nanoscale.

…describe this work to a layperson?

Here, we discuss approaches to scale down tensile testing to probe mechanical properties of materials from the millimeter to the nanometer scale.

TENSILE TESTING APPROACHES AND TECHNIQUES

There are several experimental hurdles that must be overcome to do proper tensile testing of materials in order to obtain precise mechanical property measurements. In the macro-world, the majority of these issues has been studied in detail and in many cases standardized (e.g., ASTM standards). The pertinent questions at the micro- and nanoscale become: What techniques can we simply scale down from large-scale approaches, and at what point do we need radically different methodologies to deal with reduced dimensions? The following sections systematically address the steps necessary to realize a tensile test at small scales and highlight several unique approaches that researchers in the field have developed to overcome these challenges.

The synthesis of materials with reduced dimensions (e.g., coating materials, novel nanostructures, thin films) is a burgeoning field of research. Metrology for accurate sample measurement and micro- and nanostructural characterization must be juxtaposed with synthesis and testing. These topics are de-

serving of their own attention (see, for example, Reference 1), and major progress has been made in the last decades; advances have been made in marriage with the development of novel microscopy technologies. Here the emphasis will be placed entirely on the issues and challenges pertaining to mechanical testing of small-scale materials.

Specimen Harvesting, Manipulation, and Gripping

Specimens at the larger end of the length scales covered in this overview (envelope dimensions of several mm × hundreds of μm × tens to hundreds of μm, see, e.g., Figure 1) can be handled in much the same way that conventional tensile specimens are. Sharp tweezers can often be used for manipulating specimens, and more controlled air tweezers for soft and ductile specimens. In a recent review on microscale mechanical characterization, K.J. Hemker

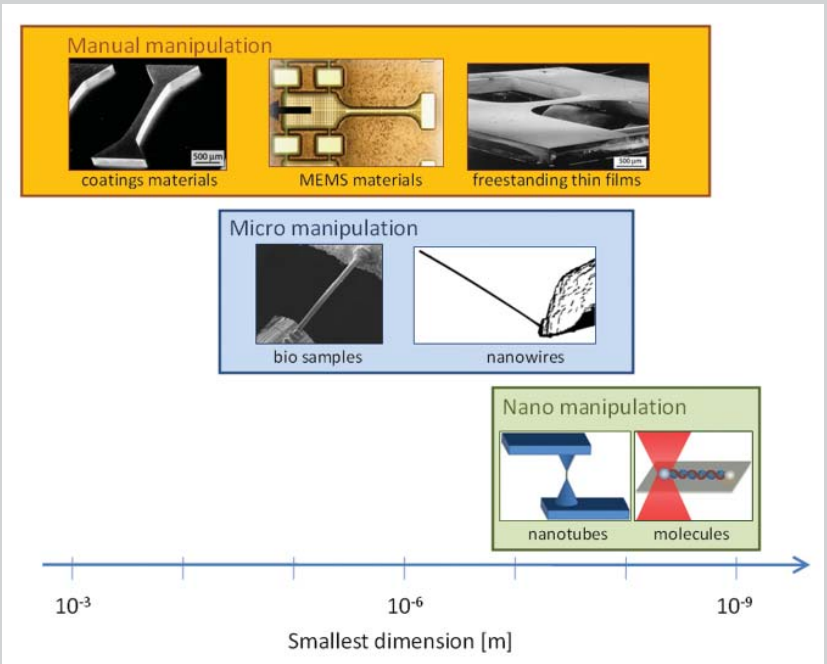

Figure 1. Specimen manipulation strategies are illustrated schematically across the length scales involved in micro- and nanotensile testing. The top row shows examples of specimens that can be handled using tweezers. The middle and bottom rows require manipulators to harvest and transfer specimens to a testing platform, and differ in the necessary motion fidelity. (LIGA Ni image reprinted, with permission, from the *Annual Review of Materials Research*, Volume 37 ©2007 by Annual Reviews. Thin film image reprinted with permission from SPIE.)

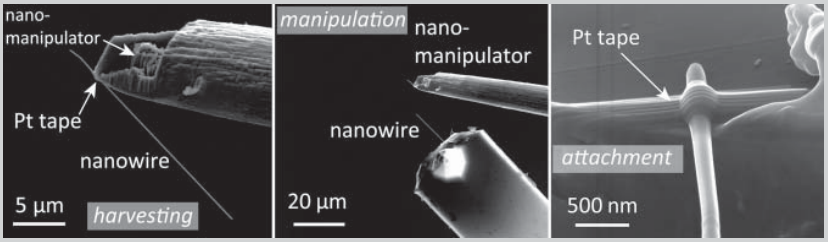

Figure 2. Scanning electron microscopy images showing strategies for harvesting, manipulating, and attaching quasi-1-D nanostructures. A nanomanipulator is operated in the SEM and can be attached to a specimen using local platinum deposition. Transfer and alignment can be accomplished by using the FIB to cut the specimen. A close-up view of platinum "tape" used for gripping during tensile testing, as deposited with the assistance of the e-beam.

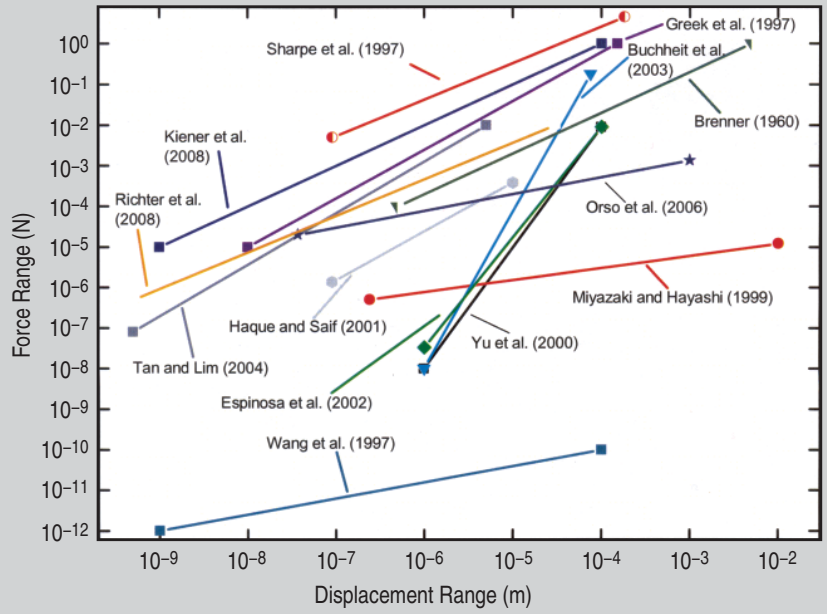

Figure 3. The force versus displacement range offered by a variety of small-scale tensile testing techniques, spanning approximately eight decades of force and displacement range.[21,30,40–43,50,60,85,92,111] The lower point represents the resolution of the system, while the upper point is the maximum allowable value. This plot gives guidelines for recommended testing approaches. (Figure courtesy of Steffen Orso.[44])

and W.N. Sharpe[2] highlighted techniques for fabricating and handling freestanding microspecimens and presented examples of the insightful results obtained from testing for a broad range of materials applications.

However, many micro- and nanoscale specimens are typically very fragile and cannot withstand the brutality of conventional handling tools (e.g., tweezers, hands). Two general categories of remedies are employed to accomplish specimen handling: mounting the specimen on a support structure that is large and/or stiff enough to handle easily with typical tools, and harvesting individual specimens from the location where they were grown, assembled, or dispersed using micro- and nanomanipulators and transferring them to a testing device. Figure 1 illustrates examples of specimen geometries as a function of size and manipulation scheme.

A support structure can easily be integrated into a microfabrication or MEMS processing scheme in order to test freestanding thin films. Both additive (e.g., deposition of layers on a substrate) and subtractive (e.g., etching through layers, removal of sacrificial layers) processes can be used in the process flow to implement a platform that consists of a thin film that is anchored to a substrate but released in the gage section. C.A. Neugebauer[3] developed such a method using gold films and a rock salt substrate as far back as 1960. D.T. Read and J.W. Dalley,[4] and later W.N. Sharpe, Jr. and colleagues,[5] extended this technique for testing films that are deposited on a silicon substrate. As shown in Figure 1, a freestanding polysilicon thin film specimen (3 μm thick) is framed by a silicon supporting structure consisting of 500 μm thick silicon grips and support strips on the periphery.[5] This die is handled easily with tweezers, and can be integrated into a tensile testing platform. Prior to testing, the support strips can be cut with a diamond-impregnated rotary tool so that the loads are only incurred by the thin film. This technique has been successfully utilized for the testing of Ti-Al-Ti,[4] polysilicon,[6] nanocrystalline aluminum,[7] gold,[8,9] SiN,[10] and SiC.[11]

An alternative method involves surface micromachining of thin-film materials on the surface of a substrate and subsequently removing sacrificial layers or etching below specimens to release the gage section, as introduced by T. Tsuchiya et al.[12] Figure 1 shows the so-called narrow thin-film specimen geometry of W.N. Sharpe et al.[13] One end of the specimen remains anchored to the substrate, while the other consists of a large paddle with arrays of patterned etch holes that allows for release from the substrate during etching. This paddle is attached to anchors that can be cut before testing using a sharp micromanipulator. The large paddle can be gripped electrostatically[12] or by gluing a stiff fiber and attaching the other end to a load cell.[13–17] One advantage of this method is the ability to test specimens in a more parallel fashion, since the alignment of the loading device needs to be accomplished only once per die. D.T. Read et al.[18] proposed an alternative paddle geometry that has been used by others[19,20] consisting of an annular ring on the free side of the specimen, allowing for a separate hook structure to apply forces to the specimen.

Co-fabrication of the specimen and testing apparatus has been proven to be an attractive strategy in situations where the materials synthesis can be integrated in the device process flow. This is particularly appealing for materials used in microelectronics, MEMS, and NEMS synthesized by vapor deposition methods, and allows for batch processing and testing of many specimens on a single wafer. Co-fabrication has the clear advantage of circumventing gripping and alignment issues by incorporating the specimen into the device fabrication using multiple photolithography masks, for example. M.A. Haque and M.T.A. Saif have co-fabricated and performed tensile testing of thin metal films as thin as 30 nm[21] and H.D. Espinosa and colleagues have employed this strategy to test polysilicon specimens and one-dimensional (1-D) nanostructures.[22]

The described strategies for specimen manipulation are not always feasible when a specimen's largest dimension is less than several tens of micrometers, as in the case of nanotubes, nanowires, nanobelts, and some biomaterials. Y. Zhu, C. Ke, and H.D. Espinosa[23] recently reviewed the state of the art of mechanical characterization of 1-D nanostructures, and point out that one of the largest challenges is the handling of extremely small specimens. Micro- and nanomanipulators can be used in conjunction with high-resolution imaging systems to locate, attach, transfer, and manipulate these structures to the desired testing platform. For example, several commercial nanomanipulators with multiple degrees of freedom are now available that make use of piezoelectric materials combined with so-called inertial drive mechanisms. These actuators exploit the difference between the static and dynamic coefficients of friction, offering sub-nanometer resolution with millimeter to centimeter ranges (examples of commercially available systems include Kleindiek Nanotechnik, Omniprobe, and Klocke Nanotechnik). By attaching fine tapered probes (typically sharpened by electropolishing, and many times re-sharpened by the focused ion beam [FIB]), tiny specimens can be manipulated and harvested with no to minimal handling damage. In situations where specimens can no longer be imaged using white-light optical microscopy, nanomanipulators can be integrated into transmission electron microscopy (TEM),[24,25] scanning electron microscopy (SEM), and/or FIB[26] environments where they can be used in conjunction with local deposition systems for specimen attachment.

Common approaches for in situ attachment include local deposition or accumulation of hydrocarbons present in the vacuum system using a focused e-beam (EBID),[27] or the local injection of a precursor gas (called a gas injection system, or GIS) that adsorbs to the sample surface and can be locally decomposed using EBID or an ion beam (IBID). The desired compound is deposited where the beam is scanned, and the reaction products are volatile and can be pumped away. This method has been utilized extensively,[28,29] and GIS systems currently exist with the capability of depositing gold, platinum, and tungsten. The GIS method has also been used for local metal deposition to grip specimens for tensile testing. For example, S. Orso et al. used IBID to deposit "fixation tape" of tungsten to individual setae from the leg of a beetle for subsequent tensile testing.[30] Figure 2 shows the manipulation and transfer of nanowires by utilizing a commercial nanomanipulator and

local platinum deposition. Limited information exists regarding the strength of these "tape" deposits given that the microstructure and corresponding properties vary wildly depending on the deposition conditions.[31] Nevertheless, this gripping method has proven to be sufficiently strong for specimens as large as several micrometers, generating forces as high as ~ 5 mN.[30]

In addition, the advent of atomic force microscopy (AFM/SPM) based techniques has spawned a new generation of tools using the atomically sharp tip as an end effector to manipulate objects as small as individual atoms.[32] This approach is often named the AFM nanorobot[33,34] and can be made more versatile by functionalizing the tip to enhance the specificity of binding to certain molecules or particles (often called chemical force microscopy). For example, S.H. Leuba et al. employed this approach to stretch single strands of chromatin and measured their mechanical response.[35]

Novel manipulation and patterning techniques have been proposed and could prove to be very useful for attachment of tensile specimens, particularly those that require high throughput or special environments (e.g., aqueous solutions, non-ambient conditions). Some examples include random dispersion of nanostructures in suspension solution onto patterned grids or by directed self-assembly to encourage pattern formation,[23] alignment using external electric fields by utilizing the dielectrophoresis effect,[36,37] and direct growth of nanostructures by patterning or manipulating growth catalyst particles in desired locations and orientations.[38,39] These methods show promise for accelerated tensile testing of materials to efficiently generate large materials properties datasets.

Actuation and Force/ Displacement Measurement

One must consider the expected forces and displacements that would be incurred when approaching micro- and nanoscale tensile testing (see Figure 3 for literature values of force and displacement ranges for a variety of testing approaches[40–44]). Other important considerations when choosing a testing apparatus are the materials properties that are desired (e.g., elastic moduli, yield strength, stress relaxation, etc.) and whether dynamic material changes (e.g., discrete deformation, yield points) are expected during testing. At larger scales, Sharpe, Hemker, and coworkers[2] showed that many microtensile testing needs can be satisfied using careful selection of commercially available components.

Actuation technologies exist that offer nanometer and sub-nanometer resolution, and others are available that offer large ranges of motion; the challenge is obtaining a system that provides high dynamic range (i.e., fine step sizes and large ranges). Piezoelectric actuators offer decided advantages in terms of resolution of motion (since the principle is based on atomic-level straining) and speed control, and can be fabricated in special stack geometries to extend the range of motion. However, piezo-based actuation systems are susceptible to direct current (DC) drift and stack designs are not always very compact, precluding use in restricted spaces (e.g., in situ experiments). High dynamic range actuators are commercially available that make use of the inertial drive mechanism mentioned previously, combining precision motion of piezoelectric materials with large travel (e.g., tens of millimeters). This motion can be accomplished using linear sliding or by a ratcheting motion of piezoelectric jaws over a finely threaded screw.

Thermal actuation has been demonstrated as a useful and stable actuation method,[45,46] which involves the coupling of electrical, thermal, and mechanical fields. A DC current is passed between external contacts connected to slender beams, which induces resistive heating along angled beams. The heat resulting from the Ohmic dissipation results in thermal expansion of the beams along their longitudinal axes and projects into rectilinear motion for actuation. The amount of force and displacement that the thermal actuator can generate is a function of the beam geometry, the angle of inclination relative to the actuation axis, the number of beams used, and the material properties of the actuator.

Once the actuation technique has been chosen, one must consider a method for measuring the tiny forces encountered in small-scale specimens. Many commercial load cells based on conventional technology such as Wheatstone bridges or internal leaf springs are available that provide the capability of measuring forces as small as several tens of micronewtons.

Flexure-based load measurement systems that rely on transverse deflection of beams perhaps offer the most versatility, since the load range can be customized to suit the testing needs simply by adjusting the geometry. This can be accomplished readily at larger scales by using CAD-based EDM or laser cutting methods, and by microfabrication or FIB milling at smaller length scales. Cantilevered beams are sensitive load sensors since they are very compliant; indeed, this point is exploited in AFM,[47] surface stress-induced chemical and biological sensing,[48] and stress evolution studies during thin-film growth.[49] For example, M.F. Yu et al.[50] used two opposing AFM cantilevers to manipulate and test multi-walled carbon nanotubes in tension. S. Gudlavaletti and colleagues[51] demonstrated the versatility of flexure-based systems by providing design considerations and constructing monolithic apparatuses to perform tensile testing at different length scales.

Several researchers promoted this technique for force measurement during tensile testing of one-dimensional nanostructures,[22,23,52] freestanding metallic thin films,[21,53] and polysilicon[22] by microfabricating testing devices that integrate actuators and load measurement devices all on a single chip. Haque and Saif[21] introduced an integrated testing device consisting of silicon beams and grips that are etched through the entire chip in order to perform in situ TEM tensile testing. They developed a new generation of testing platform,[54] as shown in Figure 4a, with some advantages including reference markers for relative displacement measurements (thus, 1-D strain) and the possibility for concurrent four-point electrical characterization. This device can be integrated easily into existing TEM straining holders and simple ex situ actuators, but requires external loading. Espinosa and co-workers[22] developed fully integrated testing platforms that rely on thermally driven actuators or capacitive structures inducing electrostatic forces (Figure 4b). Their devices require only that

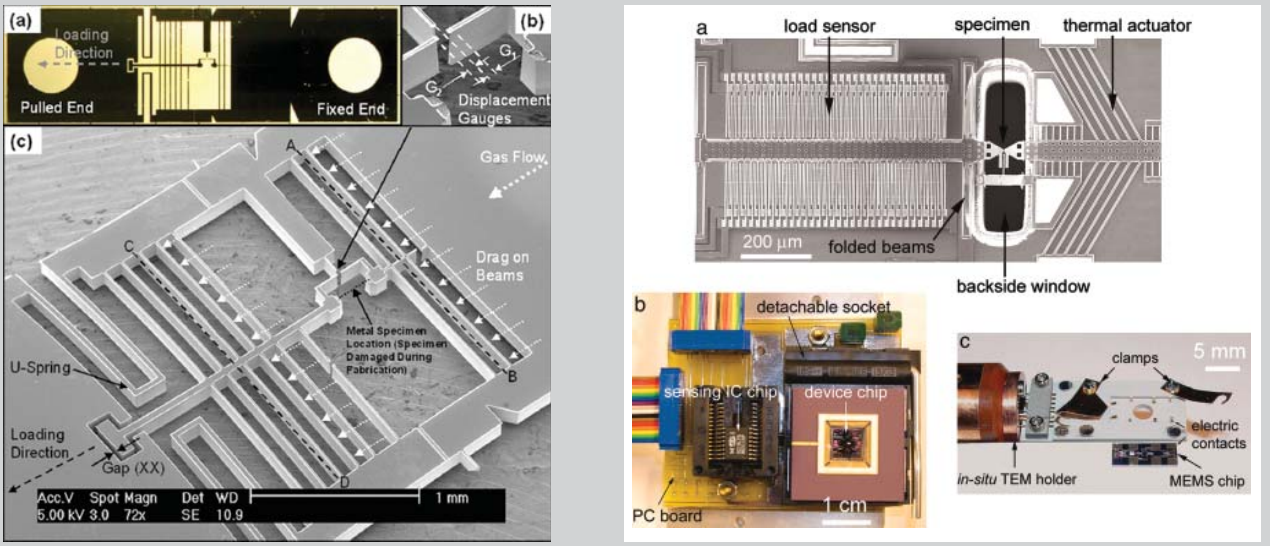

Figure 4. MEMS-based tensile testing platforms in which the specimen is co-fabricated with the testing apparatus. (a) Platform of Han and Saif,[54] which utilizes flexure beams for alignment and force measurement, and can be installed in in situ SEM or TEM straining holders. (Reused with permission from Jong H. Han, *Review of Scientific Instruments*, 77, 045102 (2006). Copyright 2006, American Institute of Physics.) (b) SEM image of platform of Espinosa et al.,[22] which has the actuator, load cell, and specimen all on-chip. Only external electrical connections are required to operate the device, and the device can also be operated in the TEM. (Copyright 2005 National Academy of Sciences, U.S.A.)

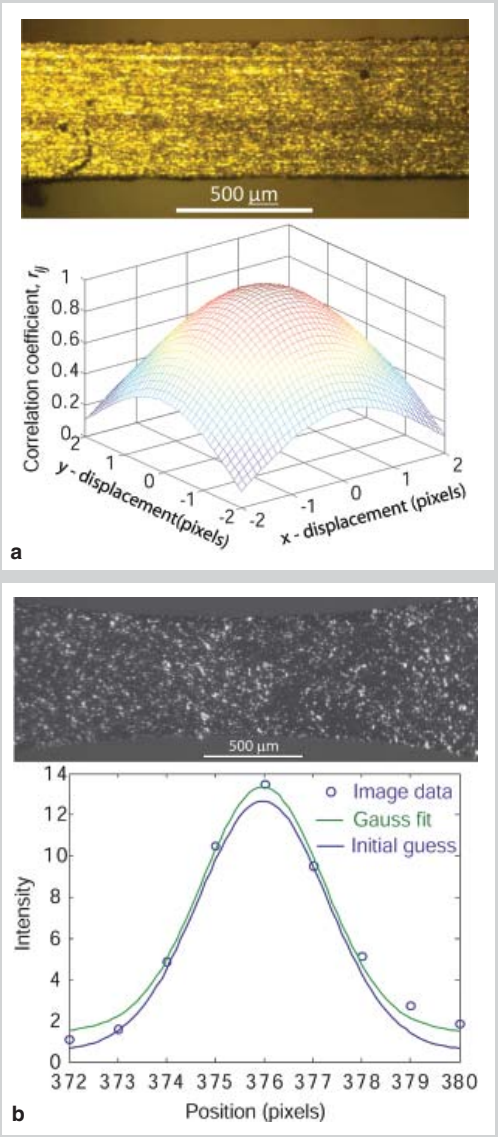

Figure 5. Examples of specimens with optimal contrast for (a) DIC and (b) DDIT non-contact strain measurement. (a) Image of a rolled Al 5053 microtensile specimen with natural surface contrast good for DIC, and corresponding correlation coefficient that is maximized during DIC procedure. (b) Image of surface of nanocrystalline aluminum submicrometer thin film decorated with SiOx particles, ideal for DDIT. A section of one particle shown as the intensity from the digital camera as a function of position. A Gauss function is fit to the raw data, and the evolution of the peak center can be tracked with sub-pixel resolution.

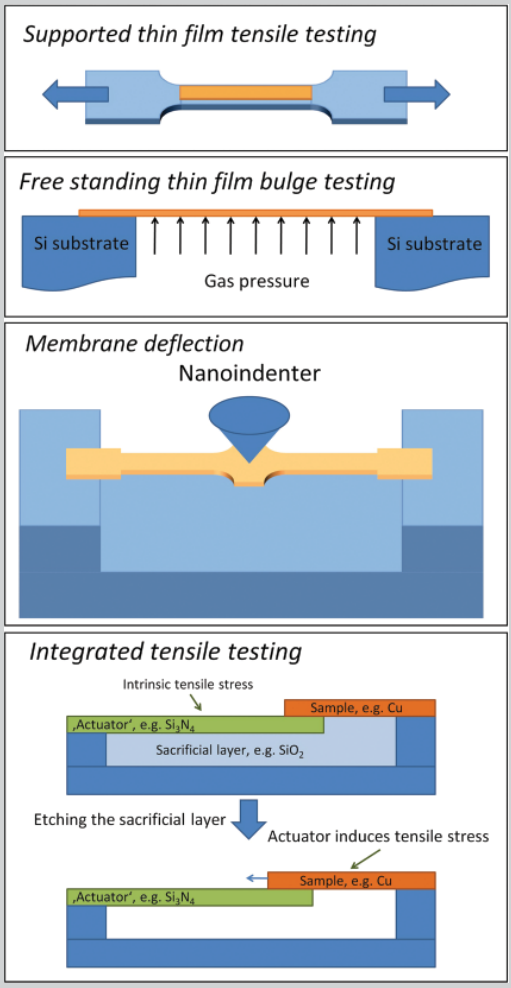

Figure 6. Examples of alternative small scale testing devices that lead to tensile stresses and strains in specimens: thin film deposited on a polymer dogbone, bulge testing of freestanding thin film, membrane deflection technique using a nanoindenter system to stretch thin films, and use of intrinsic stress in SiNx actuators in a microfabrication process flow. Subsequent etching of a sacrificial layer causes the SiNx beam to pull on the testing specimen.

electrical contacts be made to the device, which can be easily accomplished using standard wire bonding. R.S. Ruoff et al.[55] designed and implemented a flexure-based, microfabrication-realized testing platform with a novel geometry that produces displacement de-amplification from thermal actuators, resulting in precise nanometer-level control.

Nanoindentation systems are most often utilized for compression testing of materials (e.g., sharp indentation, pillar compression), but can also be utilized for small-scale tensile testing.[52] Some transducer designs rely on electromagnets for force actuation and capacitive systems for displacement measurement (see for example Reference 56 for a review on instrumented indentation), while others utilize electrostatic interactions between capacitive structures for force generation.[57] The latter systems employ a three-plate capacitor design and superimpose high-frequency antiphase alternating current (AC) signals to opposing capacitor plates to measure displacement.[57] It should be noted that both transducer designs are inherently force-controlled, but sophisticated feedback systems can be used to achieve quasi-displacement control during testing.

Focused light can also be used to apply or measure forces on small specimens. The research group of C. Bustamante[58] implemented an optical trapping system (also known as optical tweezers) to experimentally investigate the extensibility of DNA. This approach exploits the electrical field gradient produced by a focused laser beam, which interacts with and traps dielectric particles (typically glass or polymeric beads attached to biomolecules) in the center of the beam. If the bead is moved from the optical center, then a restoring force is applied to the dielectric particle due to the momentum transfer from the scattering of light, allowing for mechanical testing experiments. Position-sensitive detectors (e.g., photodiodes or CCD cameras) are placed downstream from the optical path and can detect beam displacements (at the nanometer level), while forces (as low as 10^{-13} N) are applied by either steering the beam or by precisely moving the other end of the specimen using a piezoelectric stage.[59] It should be noted that careful and tedious calibration of these systems is necessary to quantify the changing trap stiffness and displacement output.[60]

Strain Measurement

Accurate tensile testing requires direct strain measurement in the gage section[61] of the specimen and in small-scale testing this can be achieved by non-contact strain measurement methods. Notable approaches include the interferometric strain displacement gage (ISDG[62]), tracking of diffraction spots from gratings deposited on specimen surfaces,[63] digital image correlation (DIC),[16,64] and differential digital image tracking (DDIT).[15,30] These techniques also allow for the measurement of the lateral strain to measure Poisson's ratio.[5,65] Digital image correlation and DDIT have the advantage of full-field capability giving local fidelity (e.g., strain heterogeneities near grain boundaries).[66] These techniques measure the strain even after tensile necking extending the measureable stress-strain behavior beyond the maximum engineering stress.[65] In the case of in situ tensile testing, DIC and DDIT are ideal methods for strain measurement, as the SEM,[66–68] FIB,[30] or AFM[16] can be used as image sources during the test. Thus, quantitative information can be extracted in addition to imaging the deformation mor-

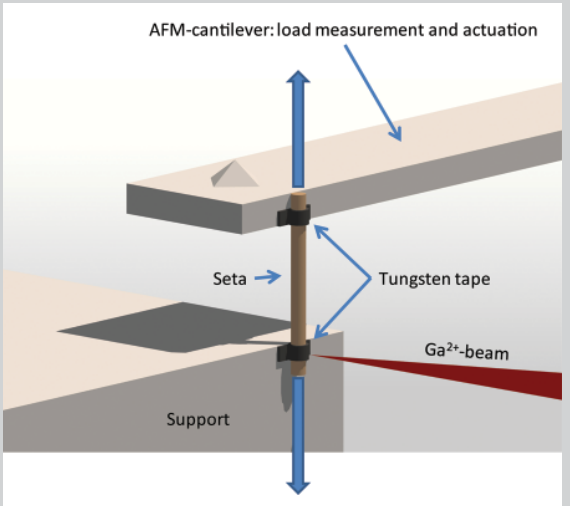

a

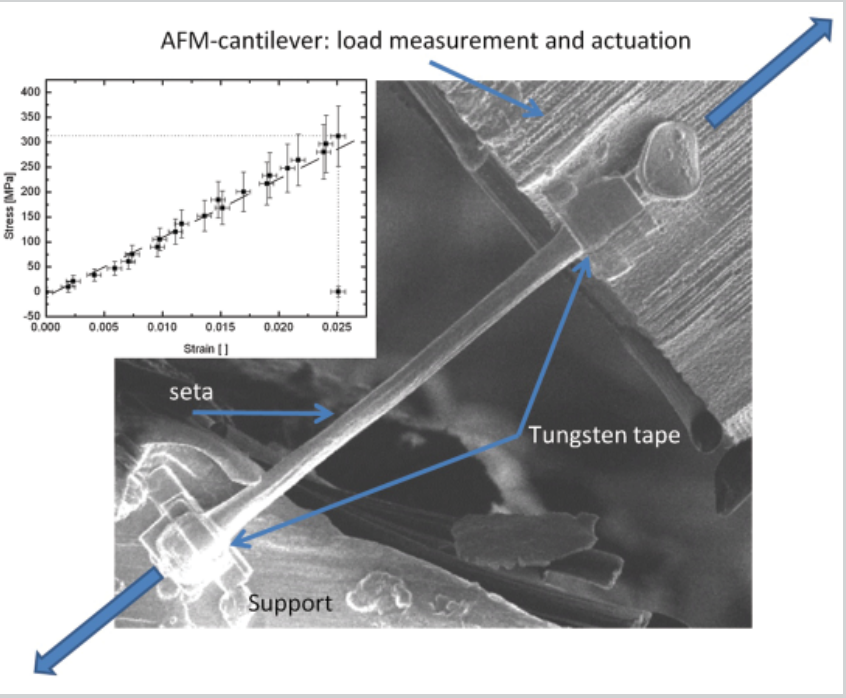

b

Figure 7. In situ FIB tensile testing approach for individual seta from the leg of a beetle. (a) Illustration showing AFM cantilever load measurement device, specimen, and attachment points. (b) FIB image of a specimen during testing. Inset shows stress strain behavior. Strain was measured locally using DDIT of captured images.

phology during testing.

The basic premise of DIC is as follows, and a representative image demonstrating good surface contrast on a microspecimen is shown in Figure 5a. The correlation coefficients of subsets of consecutive images (typically between 10×10 to 40×40 pixels^2) are calculated and plotted versus their position. Biquadratic functions, for instance, can be used to locate the maximum correlation coefficient (with sub-pixel resolution) that is representative of the optimal fit between the subsets of the two images (Figure 5a). Differential digital image tracking requires intensity peaks in the source images that can be tracked by a peak fitting algorithm (Figure 5b). This method can achieve a resolution of up to a thousandth of a pixel, which allows for good strain fidelity even in the absence of many pixels (e.g., AFM images with ~200×200 pixels^2 resulting in strain resolutions of up to $\Delta\varepsilon = 10^{-5}$). Ultimately, the resolution of DIC and DDIT primarily hinge on the noise present in the imaging system. Differential digital image tracking is typically less susceptible to local image noise since features are tracked that span multiple pixels. Free MATLAB® code for DIC and DDIT is available online.[69]

Indirect Tensile Testing Methods

The focus of this paper is on instrumented tensile testing in which the uniaxial load and displacement are measured directly and independently. However, several small-scale testing methods have been reported that induce tensile loads in specimens and are capable of measuring full stress-strain curves. Notable examples include plane-strain bulge testing,[70] the membrane deflection technique,[71] and an on-chip residual stress-induced actuation method.[72] These methods are illustrated in Figure 6.

Co-deforming a thin film with a polymer substrate (Figure 6) is another way to stabilize fragile specimens and is also of technological interest for use in flexible electronics for displays and active textiles. Several researchers have utilized this approach to study the tensile behavior of films as thin as 20 nm.[73–77] Furthermore, in situ x-ray diffraction can be used to quantify stress evolution in crystalline materials since the total force cannot be directly related to stress in the thin film. Upon analyzing the diffraction patterns, one can calculate the elastic multi-dimensional lattice strains from interplanar crystalline spacings and combining multiple measurements in orientation space. These quantities can be related via careful analysis to the stress in the crystal via the elastic constants.[78,79] The influence of Poisson contraction and time-dependent relaxation of the underlying polymer can therefore be mitigated as employed extensively by H. Hommel and O. Kraft,[73] P.A. Gruber et al.[80,81] for continuous films and S. Olliges et al. for structured films.[82]

Bulge testing involves pressurizing a freestanding thin film that is clamped at its edges to induce tensile stresses in the membrane (Figure 6); the pressure and deflection of the membrane are measured independently, as introduced by J.J. Vlassak and W.D. Nix.[70] This has been applied to the testing of various metal films with and without passivation layers.[83,84]

The membrane deflection technique was developed by H.D. Espinosa and colleagues,[71,85] where a long doubly clamped freestanding thin film is pushed in its center using a nanoindenter (Figure 6). Given the lack of bending stiffness in thin films, the transverse loading translates to tension in the membranes on either side of the loading point. Force is measured by the nanoindenter,

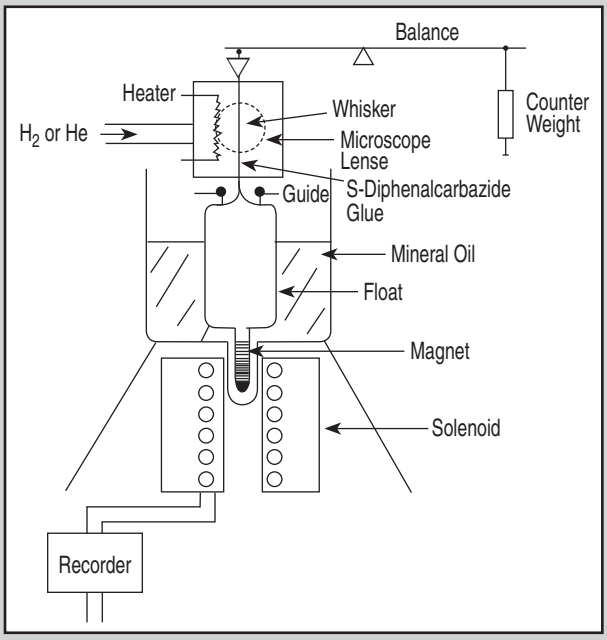

a

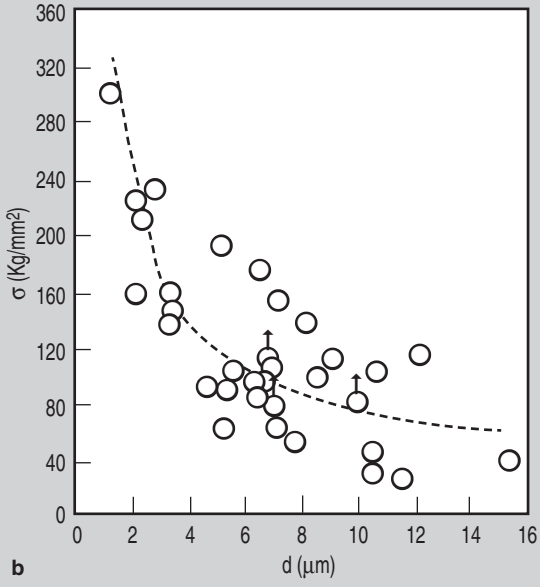

b

Figure 8. Tensile testing of single crystalline metallic microwhiskers.[92] (a) Experimental tensile testing constructed by Brenner and (b) results of copper whisker fracture strength as a function of whisker size, showing clear size dependence. (Reused with permission from S.S. Brenner, *Journal of Applied Physics*, 27, 1484 (1956). Copyright 1956, American Institute of Physics.)

and the vertical deflection can be measured using an interferometer.

Lastly, N. André et al.[72] developed a tensile testing technique which can be integrated into a MEMS or microelectronics process, where the actuation is carried out by residual stresses in SiN_x. During etching of a sacrificial layer that initially holds the layers in place, the intrinsic stress in the SiN_x actuator pulls on the sample as illustrated in Figure 6, and by integrating several of these structures with different actuator lengths, the actuated displacement can be varied. The load on the sample can be measured by the difference in displacement of each actuator compared to a stress-free state. Each actuator-sample structure represents one data point on the stress-strain curve.

INSIGHTS GAINED FROM SMALL-SCALE TENSILE TESTING

Micro- and nanotensile testing have helped further our understanding of how small volumes of materials deform, as shown in the following examples.

Tensile Testing of Biological Attachment Devices

Biologically inspired adhesion systems have recently attracted significant attention as a replacement for chemistry-based adhesives, tapes, and industrial grippers. Some insects and geckos use hierarchical hairy attachment systems of brush-like structures as small as 200 nm to reversibly adhere to walls and chase down their prey. Several researchers have shown that van der Waals interactions and capillary forces provide the observed adhesion[86–89] and have studied the related scaling laws. The findings can be used to identify the optimum geometric and materials properties via adhesion maps.[90,91] Measurements of the mechanical properties of these small structures is necessary for efficient design yet challenging, as the diameters of setae scale from several micrometers down to 200 nm with lengths between several micrometers and 100 μm.

Orso et al.[30] were successful in utilizing a micromanipulator mounted into an FIB microscope to separate, cut, and fix single setae from the leg of a gastrophysa viridula (beetle) and carry out in-situ microtensile tests. The experimental setup for tensile testing is shown in Figure 7. The load was measured by an AFM tip attached to the micromanipulator and the setae were glued by tungsten tapes deposited using IBID to a metal block and the AFM tip. The strain was calculated using DDIT from the FIB micrographs obtained continuously throughout the test.

The measured Young's modulus of the gastrophysa viridula setae was 13.3 ±1 GPa and the reported ultimate strength was 310 ± 60 MPa. The mechanical behavior showed almost ideal elastic behavior (inset of Figure 7) and compares with properties of chitin fiber-reinforced composite materials. The authors pointed out that the Young's modulus of biological materials is often higher in vacuum than under normal atmospheres due to dehydration. This study set a precedent for extracting the properties of biological attachment systems, which aids designers in selecting bio-mimicking materials and optimizing structural design for the development of artificial attachment systems.

Size-Dependent Plastic Behavior in Single-Crystalline Metals

More than fifty years ago, S.S. Brenner[92] published seminal work on the deformation of microscale single crystals to convincingly demonstrate that size indeed does matter, and deformation behavior of metals can be altered by simply changing the external specimen size. He reported tensile testing results of copper, iron, and silver whiskers ranging in diameter from approximately 1 μm to 15 μm and 1 mm to 4 mm in length that were grown using reduction of halides and tested in the apparatus shown in Figure 8a. Stress-strain behavior was characterized as strong, but with limited plastic flow, and pronounced deviations from linear elasticity were measured in the iron whiskers that were attributed to strains that exceeded the linear elastic limit of Hookian elasticity.[92] He showed that the ultimate strength of the whiskers showed prominent size dependence (Figure 8b), with critical resolved shear strengths falling closely to the lower estimate for the ideal strength of these metals in the case of the smallest whiskers.

Brenner followed up this work[93,94] with more results on copper, silver, and gold whiskers using a modified setup that prevented the load train from exhibiting large deflections at the point of a large excursion event. This improvement allowed for the elucidation of sharp yield points, followed by regions of "easy glide" at a fraction of the yield point stress (as little as 10%) that was characterized by Lüders band propagation. Interestingly, the yield point exhibited size dependence, while the lower flow region did not. These observations, coupled with experiments that showed that a fractured whisker with less volume could be re-tested to recoup an even higher yield point, indicated that these whiskers had minimal starting defects and extreme stresses were required to nucleate defects. The nucleation stress was dependent on the probability of finding a critical defect of a critical size; thus, the measured volume or surface area dependence, akin to the classic experiments on the deformation of glass rods.[95] The results of this work highlighted the importance of discrete defects in small volumes, catalyzing the mantra of "smaller is stronger," a departure from our conventional wisdom of continuum descriptions of plasticity.

Recently, micro- and nanocompression has been developed by M.D. Uchic and colleagues[96,97] to study size-dependent (e.g., intrinsic and extrinsic size effects) and site-specific (e.g., local properties of composites, multi-phase materials, etc.) properties of materials, as discussed in a companion paper in this issue. This approach makes use of an FIB to fabricate small structures with control of size, and experimental studies on the deformation of face-centered cubic (fcc),[96,98–102] body-centered cubic (bcc),[103,104] and amorphous metals[105–107] have been conducted. Crystalline metals have shown a clear size dependence on the yield or flow stress. A vigorous debate has taken place to explain the underlying deformation mechanisms responsible for the size effect and departure from bulk behavior that have been revealed by this technique. The prevailing mechanistic explanations for fcc materials invoke the importance of dislocation source nucleation and activation,[99] source truncation by free

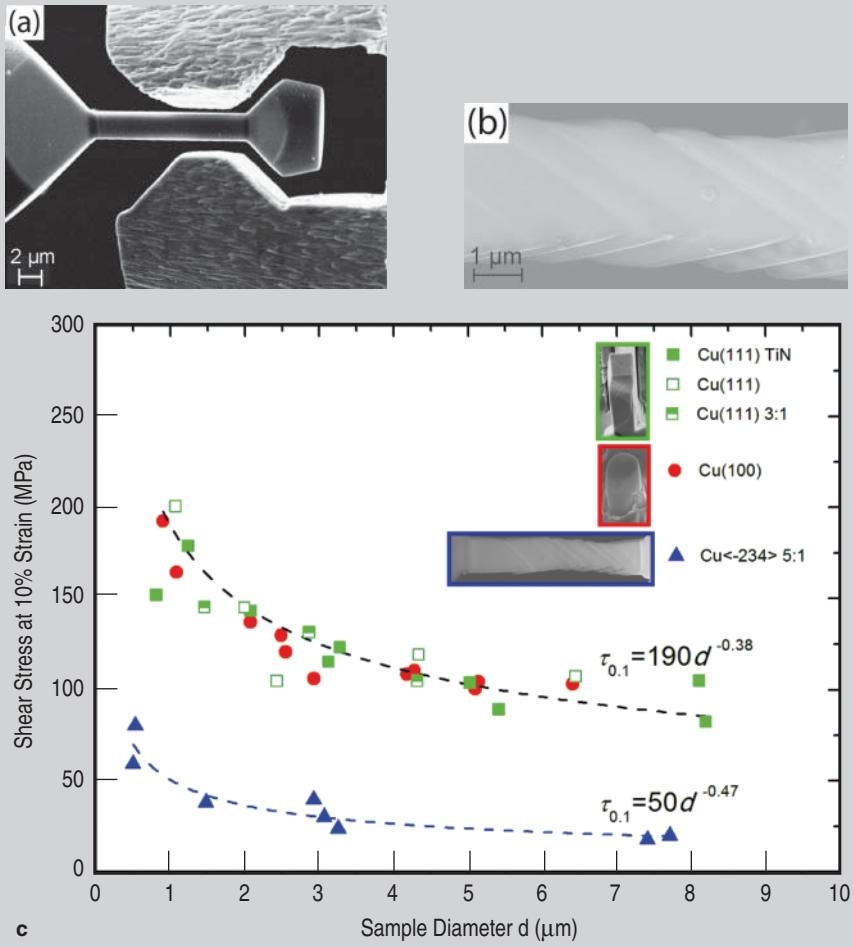

Figure 9. In situ SEM tensile testing of FIB fabricated single-crystalline microtensile specimens.[111] (a) The specimen and the grip are fashioned using the FIB to carve a gage section and a negative mold for gripping. (b) Deformed tensile specimens with sizes ranging from 0.5 to 8 μm demonstrated discrete slip band formation on the surfaces. (Reprinted from Reference 111 with permission from Elsevier.) (c) Resolved shear stress at 10% strain vs. sample diameter, showing distinct strengths and scaling depending on the deformation constraint, imposed by either testing in compression or changing the aspect ratio of the specimen.[110] (Reprinted from Reference 110 with permission from Elsevier.)

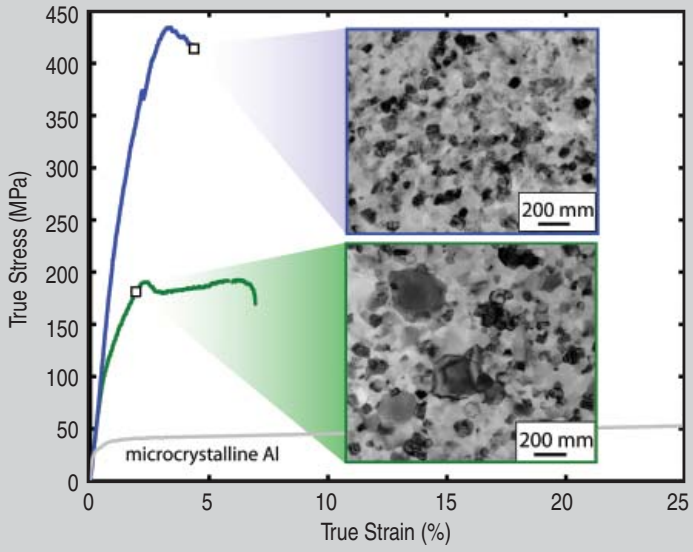

Figure 10. Microtensile stress-strain curves for submicrometer nanocrystalline aluminum thin films showing two distinct behaviors.[7] The curve with the highest strength, gradual deviation from plasticity, and limited ductility is representative of a specimen that maintains its nanocrystalline grain size. By contrast, specimens observed to undergo stress-assisted room-temperature grain growth exhibit lower yield strengths and regions of extended plasticity.

surfaces and subsequent exhaustion,[108] and dislocation starvation of defect-free crystals.[109] These compression experiments have revealed significant insight on the deformation of small metallic volumes, but the effect of the compressive loading modality (e.g., heterogeneous stress state from column tapering, stress concentrations arising from friction between the punch and the specimen, poorly defined boundary conditions) on the observed size effect is still elusive.

Recently, D. Kiener and colleagues[110,111] and Uchic et al.[97] developed in situ SEM methods for tensile testing of single-crystalline metallic specimens fabricated using FIB methods. The specimen and gripping configuration from Kiener et al. is shown in Figure 9, and was used for tensile specimens with sizes ranging from 0.5 μm to 8 μm. The major finding of this work is that tensile specimens with aspect ratios (length to width ratio) of 2:1 or higher exhibited yield strengths that were approximately three times lower than equivalent compression experiments using the same FIB parameters and experimental testing apparatus (Figure 9c). An extension of this work[110] demonstrated that reversing the loading of a tensile specimen into compression does not alter the yield strength; no tension-compression asymmetry was measured in these specimens. However, lowering the aspect ratio of the tensile specimens to mimic that of the compression pillars returns the strength to that measured from compression. Moreover, pronounced hardening is measured for low-aspect-ratio specimens. This point is attributed to the interaction and constraint of dislocation glide planes with the boundaries of the specimen, which will induce dislocation pile-ups leading to measurable hardening and a size dependence of the strength. Taken as a whole, these experiments emphasize the importance of boundary conditions, particularly in single-crystal deformation, and inspire the need to deconvolute the role of testing artifacts from intrinsic size-dependent response.

A bridge between the experiments of Brenner and the micro- and nanocompression and microtension experiments of specimens fabricated using the FIB is still missing, given that microwhiskers

demonstrated strengths close to the ideal strength while similarly sized specimens fabricated using the FIB show strengths significantly far away from this upper bound. Recent experiments from H. Bei and colleagues[112] provide evidence to suggest that the difference in measured strength lies primarily on the pre-existing defect structures in the material. In those works, molybdenum alloy compression pillars were fabricated by directional solidification of a eutectic and subsequent etching of the matrix, and no use of the FIB was needed. These pillars were presumably defect-free and demonstrated strengths near the calculated theoretical strength of molybdenum and no size dependence was measured. Size-dependent behavior and lower strengths returned when these specimens were irradiated with the FIB using conditions that emulate pillar preparation,[113] or when the composite material was pre-strained prior to etching and testing of the molybdenum alloy pillars.[114] Recent experiments by G. Richter et al.[52] reporting tensile testing of defect-free copper nanowhiskers complement the experiments of Bei and Brenner, also show a departure from pillar behavior, and give strengths at or near the ideal strength. The emerging picture suggests that the presence or absence of pre-existing defects in small volumes greatly contributes to the measured mechanical response of the material, and points to the need for thorough nanostructural characterization to accurately predict deformation and strength.

Deformation Mechanisms in Nanocrystalline Metals

Small-scale tensile testing has also made significant gains toward the understanding of deformation behavior of nanocrystalline metals, where the internal length scale given by the grain size defines the mechanical response. It is now generally accepted that nanocrystalline metals exhibit high strength and limited ductility in comparison with their coarse-grained counterparts, and conventional dislocation descriptions of crystal plasticity are abated when the grain size is reduced below approximately 100 nm. Elucidating the new mechanisms to accommodate plasticity that take over at reduced length scales has been the subject of vigorous research activity, along with several reviews (see, for example References 115–117). Proposed mechanisms that contribute to measurable global plastic strains include partial dislocation emission and subsequent absorption from grain boundaries, deformation twinning, grain boundary sliding, enhanced grain boundary diffusion, and grain boundary migration. The common denominator in all of these processes is that the large fraction of interfaces plays a large role in governing deformation.

Microtensile testing has been instrumental in characterizing the mechanical behavior of nanocrystalline metals,[118–120] primarily since large, fully dense volumes of these materials are difficult to synthesize, thus precluding the use of conventional tensile testing. For example, microtensile testing coupled with post-mortem TEM[118] and in situ x-ray diffraction[119] revealed that plastic deformation in nanocrystalline aluminum and nickel does not leave stored dislocation content in the interior of the grain as one would expect in microcrystalline materials. These studies helped form the currently accepted wisdom that grain boundaries serve as both the source and sink for dislocations in nanocrystalline metals.

In parallel, nanostructured materials are encountered in many thin film, MEMS, and NEMS applications, as the film deposition methods often synthesize material with nanoscaled grains. Freestanding thin film microtensile testing has been employed to measure yield strength, elastic moduli, hardening, and ductility of vapor-deposited nanocrystalline materials.[7,63] Room-temperature mechanical characterization of freestanding submicrometer aluminum thin films with thicknesses between 100 nm and 400 nm by D.S. Gianola and colleagues[7,65,121] have demonstrated that nanostructures can be unstable under the influence of stress, even those that demonstrate good thermal stability. Two general classes of deformation were uncovered as shown in Figure 10, briefly characterized as either strong with limited ductility and a stable microstructure or intermediate strengths with "extended" ductility and an evolving microstructure. The occurrence of stress-driven high-angle grain boundary migration was correlated to the content of impurities present during deposition.[122] Characteristics of the growth were not commensurate with conventional descriptions of grain growth[123] and instead appear to be in line with the notion of shear stress-driven coupled motion of both high- and low-angle grain boundaries, as postulated by J.W. Cahn and co-workers.[124,125]

CONCLUSIONS

Tensile testing at small size scales is an attractive field of research and technology since the output is directly interpretable, without recourse to complex models. Experimental techniques have advanced and become commercially available, enabling instrumented testing in an increasingly controlled manner. The most important developments are the availability of easy-to-use non-contact strain measurements and small scale actuators and transducers, combined with sensors of high fidelity and dynamic range.

Ultimately, engineers of all disciplines want predictive models of physical phenomena. Extracting materials properties across the length scale spectrum will give us physically based and technologically relevant models. Understanding the fundamental response of the building blocks of complex systems, coupled with a good understanding of physical constraints, will allow for the possibility of true predictive capability and intelligent engineering design. Equipped with the hierarchical knowledge of deformation at all length scales, one can push the limits of materials properties space[126] by synergistically combining materials behavior in a hybrid manner.

OUTLOOK

While the design of small-scale applications can often be based solely on elastic and plastic properties drawn from tensile testing, requirements during lifetime will be multi-faceted and lifetime can only be predicted if we understand the physical mechanisms at all scales. The various stimuli are inherently coupled and the materials properties should be measured in environments that emulate real use (e.g., integrated circuits, photovoltaics, fuel cells, advanced batteries). Short diffusion paths,

multiaxial stress states, cyclic loading, and elevated temperature have distinct implications at different length scales and generate the need for intensive investigations. Fatigue in pure thin films has been under investigation for some time now[127–129] and studies have found that thinner films can show higher lifetimes, which is a promising result. Tensile testing at elevated temperature is still limited although MEMS materials have been tested,[130] but reliable temperature control is still challenging and new concepts are needed if one desires creep testing. Advancements in coupled mechanical measurements techniques (e.g., coupled with thermal, electrical, photonic, or chemical loads) at small length scales are promising and represent an exciting arena for research. Transient tests do offer the opportunity to probe thermally activated processes and can generate new insights on active defect mechanisms.

Round-robin tensile tests, in which multiple laboratories with distinct testing capabilities collaboratively test batches of specimens to interrogate the uncertainty of measurement techniques, offer a possibility to formulate testing protocols and standardization. Tensile techniques at decreasingly small scales are still in development stages, but the ultimate goal should be to achieve testing standards commensurate with those at larger scales. Research laboratories should unite to ensure reliable and repeatable results.

Many systematic small-scale tensile testing studies have converged to the following answer: The elastic properties of fully dense microspecimens are similar to those of their bulk counterparts, as long as the effects of texture, anisotropy, and porosity are properly accounted for (see, for example, polysilicon used in MEMS[2]). Conclusive experimental evidence that demonstrates the effects of surface stress on both the elastic and plastic properties of materials with nanometer dimensions is elusive. Careful and systematic tensile testing can offer significant insight here and represents a direct way of measuring such effects.

ACKNOWLEDGEMENTS

The authors would like to thank the cast of characters that inspired their interest in small-scale mechanical testing; in particular our mentors Kevin J. Hemker and William N. Sharpe, Jr., from whom we learned the science and art of microtensile testing. C.E. would like to acknowledge financial support from the Deutsche Forschungsgemeinschaft. D.S.G. acknowledges support from an Alexander von Humboldt Postdoctoral Fellowship.

References

1. Y. Gogotsi, editor, *Nanomaterials Handbook* (Oxford, U.K.: Taylor and Francis, Inc., 2006).
2. K.J. Hemker and W.N. Sharpe, *Annual Review of Materials Research*, 37 (1) (2007), pp. 93–126.
3. C.A. Neugebauer, *Journal of Applied Physics*, 31 (6) (1960), pp. 1096–1101.
4. James W. Dally and David T. Read, *JMR*, 8 (1993), pp. 1542–1549.
5. W.N. Sharpe, Jr. et al., *Micro Electro Mechanical Systems, 1997 (MEMS '97)* (Piscataway, NJ: IEEE, 1997), pp. 424–429.
6. K.J. Hemker et al., *Journal of Microelectromechanical Systems*, 10 (3) (2001), pp. 317–326.
7. D.S. Gianola et al., *Acta Materialia*, 54 (8) (2006), pp. 2253–2263.
8. R.D. Emery and G.L. Povirk, *Acta Materialia*, 51 (7) (2003), pp. 2067–2078.
9. W.N. Sharpe et al., unpublished work (2008).
10. R.L. Edwards, G. Coles, and W.N. Sharpe, Jr., *Experimental Mechanics*, 44 (1) (2004), pp. 49–54.
11. C.A. Zorman et al., *Journal of Microelectromechanical Systems*, 14 (4) (2005), pp. 664–672.
12. T. Tsuchiya et al., *Micro Electro Mechanical Systems, 1997 (MEMS '97)* (Piscataway, NJ: IEEE, 1997), pp. 529–534.
13. W.N. Sharpe, K.T. Turner, and R.L. Edwards, *Experimental Mechanics*, 39 (3) (1999), pp. 162–170.
14. W.N. Sharpe et al., *Proceedings of IMECE 2006, 2006 ASME International Mechanical Engineering Congress and Exposition* (New York: ASME, 2006), p. 13290.
15. W.N. Sharpe et al., *Experimental Mechanics*, 47 (5) (2006), pp. 649–658.
16. Ioannis Chasiotis and Wolfgang Knauss, *Experimental Mechanics*, 42 (1) (2002), pp. 51–57.
17. S.A.I. Johansson and S. Greek, *Micromachined Devices and Components III, V*olume 3224 (Bellingham, WA, SPIE, 1997), pp. 344–351.
18. D.T. Read et al., *Scripta Materialia*, 45 (5) (2001), pp. 583–589.
19. G. Coles et al., *Mechanical Properties of Structural Films,* ed. C.L. Muhlsteom and S.B. Brown (West Conshohocken, PA: ASTM, 2001), pp. 3–15.
20. B.L. Boyce et al., *Journal of Microelectromechanical Systems*, 16 (2) (2007), pp. 179–190.
21. M.A. Haque and M.T.A. Saif, *Scripta Materialia*, 47 (12) (2002), pp. 863–867.
22. Y. Zhu and H.D. Espinosa, *Proceedings of the National Academy of Sciences of the United States of America*, 102 (41) (2005), pp. 14503–14508.
23. Y. Zhu, C. Ke, and H.D. Espinosa, *Experimental Mechanics*, 47 (1) (2007), pp. 7–24.
24. J. Cumings and A. Zettl, *Science*, 289 (5479) (2000), pp. 602–604.
25. P. Poncharal et al., *Science*, 283 (5407) (1999), pp. 1513–1516.
26. P.A. Williams et al., *Applied Physics Letters*, 80 (14) (2002), pp. 2574–2576.
27. H.W.P. Koops et al., *Japanese Journal of Applied Physics Part 1-Regular Papers Short Notes & Review Papers*, 33 (12B) (1994), pp. 7099–7107.
28. F.A. Stevie and L.A. Giannuzzi, editors, *Introduction to Focused Ion Beams: Instrumentation, Theory, Techniques and Practice* (New York: Springer, 2005).
29. C.A. Volkert and A.M. Minor, *MRS Bulletin*, 32 (5) (2007), pp. 389–395.
30. S. Orso et al., *Advanced Materials*, 18 (7) (2006), pp. 874–877.
31. H. Hiroshima et al., *Japanese Journal of Applied Physics Part 1-Regular Papers Short Notes & Review Papers*, 38 (12B) (1999), pp. 7135–7139.
32. D.M. Eigler and E.K. Schweizer, *Nature*, 344 (6266) (1990), pp. 524–526.
33. D. Nyyssonen, L. Landstein, and E. Coombs, *Journal of Vacuum Science & Technology B*, 9 (6) (1991), pp. 3612–3616.
34. M. Sitti and H. Hashimoto, *Advanced Robotics*, 13 (4) (1999), pp. 417–436.
35. M.A. Karymov et al., *Single Molecules*, 1 (2) (2000), pp. 185–192.
36. Yu Huang et al., *Science*, 291 (5504) (2001), pp. 630–633.
37. D.L. Fan et al., *Applied Physics Letters*, 85 (18) (2004), pp. 4175–4177.
38. Jing Kong et al., *Nature*, 395 (6705) (1998), pp. 878–881.
39. R. He et al., *Advanced Materials*, 17 (2005), pp. 2098–2102.
40. T.E. Buchheit et al., *Journal of Materials Science*, 38 (20) (2003), pp. 4081–4086.
41. W.N. Sharpe, B. Yuan, and R.L. Edwards, *Journal of Microelectromechanical Systems*, 6 (3) (1997), pp. 193–198.
42. E.P.S. Tan and C.T. Lim, *Review of Scientific Instruments*, 75 (8) (2004), pp. 2581–2585.
43. Hiroshi Miyazaki and Kozaburo Hayashi, *Biomedical Microdevices*, 2 (2) (1999), pp. 151–157.
44. S. Orso, "Structural and Mechanical Investigations of Biological Materials using a Focused Ion Beam Microscope" (Ph.D. thesis, Universität Stuttgart, 2005).
45. H.D. Espinosa, Y. Zhu, and A. Corigliano, *J. Micromech. Microeng.*, 16 (2006), pp. 242–253.
46. A.A. Geisberger et al., *Journal of Microelectromechanical Systems,* 12 (4) (2003), pp. 513–523.
47. G. Binnig, C.F. Quate, and Ch. Gerber, *Phys. Rev. Lett.*, 56 (9) (1986), pp. 930–933.
48. V. Nickolayet al., *Review of Scientific Instruments*, 75 (7) (2004), pp. 2229–2253.
49. K. Kinosita et al., *Japanese Journal of Applied Physics*, 6 (1967), pp. 42–53.
50. M.F. Yu et al., *Science*, 287 (5453) (2000), pp. 637–640.
51. S. Gudlavalleti, B. Gearing, and L. Anand, *Experimental Mechanics*, 45 (5) (2005), pp. 412–419.
52. G. Richter et al., "Ultra High Strength Single Crystalline Nano-Whiskers Grown by Physical Vapour Deposition" (unpublished work, 2009).
53. M.A. Haque and M.T.A. Saif, *Proceedings of the National Academy of Sciences of the United States of America*, 101 (17) (2004), pp. 6335–6340.
54. J.H. Han and M.T.A. Saif, *Review of Scientific Instruments*, 77 (4) (2006), DOI:10.1063/1.2188368 .
55. Shaoning Lu et al., *Review of Scientific Instruments*, 75 (6) (2004), pp. 2154–2162.
56. S. Rajagopalan and R. Vaidyanathan, *JOM*, 54 (9) (2002), pp. 45–48.
57. B. Bhushan et al., *Philosophical Magazine A*, 74 (1996), pp. 1117–1128.
58. S.B. Smith, Y.J. Cui, and C. Bustamante, *Science*, 271 (5250) (1966), pp. 795–799.
59. D.G. Grier, *Nature*, 424 (6950) (2003), pp. 810–816.
60. M.D. Wang et al., *Biophysical Journal*, 72 (3) (1997), pp. 1335–1346.
61. *Standard Test Methods for Tension Testing of Metallic Materials* (West Conshohocken, PA: ASTM, 2004).
62. W.N. Sharpe, *NASA Technical Memorandum (1989),* p. 101638.
63. Haibo Huang and F. Spaepen, *Acta Materialia*, 48 (12) (2000), pp. 3261–3269.
64. K.J. Hemker, B.G. Mendis, and C. Eberl, *Materials Science and Engineering A-Structural Materials Prop-*

erties Microstructure and Processing, 483 (2008), pp. 727–730.
65. D.S. Gianola et al., *Advanced Materials*, 20 (2008), pp. 303–308.
66. Nicholas Biery, Marc deGraef, and Tresa Pollock, *Metallurgical and Materials Transactions A*, 34 (10) (2003), pp. 2301–2313.
67. M. Sutton et al., *Experimental Mechanics*, 47 (6) (2007), pp. 775–787.
68. M. Sutton et al., *Experimental Mechanics*, 47 (6) (2007), pp. 789–804.
69. C. Eberl, D.S. Gianola, and R. Thompson, *MatLab Central* (Natick, MA: The Mathworks, Inc., 2006), File ID:12413.
70. J.J. Vlassak and W.D. Nix, *JMR*, 7 (1992), pp. 3242–3249.
71. H.D. Espinosa, B.C. Prorok, and B. Peng, *Journal of the Mechanics and Physics of Solids*, 52 (3) (2004), pp. 667–689.
72. N. André et al., *Microelectronic Engineering*, 84 (11) (2007), pp. 2714–2718.
73. M. Hommel and O. Kraft, *Acta Materialia*, 49 (19) (2001), pp. 3935–3947.
74. F. Macionczyk and W. Bruckner, *Journal of Applied Physics*, 86 (9) (1999), pp. 4922–4929.
75. Z. Suo et al., *Applied Physics Letters*, 87 (16) (2005), pp. 1–3.
76. N.S. Lu et al., *Applied Physics Letters*, 91 (22) (2007), p. 221909.
77. M.R. Begley and H. Bart-Smith, *International Journal of Solids and Structures*, 42 (18-19) (2005), pp. 5259–5273.
78. J. Bohm et al., *Review of Scientific Instruments*, 75 (4) (2004), pp. 1110–1119.
79. U. Welzel et al., *Journal of Applied Crystallography*, 38 (1) (2005), pp. 1–29.
80. P.A. Gruber et al., *JMR*, 23 (2008), pp. 2406–2419.
81. Patric A. Gruber et al., *Acta Materialia*, 56 (8) (2008), pp. 1876–1889.
82. Sven Olliges et al., *Acta Materialia*, 55 (15) (2007), pp. 5201–5210.
83. Y. Xiang and J.J. Vlassak, *Acta Materialia*, 54 (20) (2006), pp. 5449–5460.
84. L. Nicola et al., *J. Mechanics and Physics of Solids*, 54 (10) (2006), pp. 2089–2110.
85. B.C. Prorok, H.D. Espinosa, and M.A. Fischer, *J. Mechanics and Physics of Solids*, 51 (2003), pp. 41–67.
86. Autumn Kellar et al., *Nature*, 405 (6787) (2000), pp. 681–685.
87. Autumn Kellar et al., *Proceedings of the National Academy of Sciences of the United States of America*, 99 (19) (2002), pp. 12252–12256.
88. Gerrit Huber et al., *Proceedings of the National Academy of Sciences of the United States of America*, 102 (45) (2005), pp. 16293–16296.
89. Gerrit Huber et al., *Acta Biomaterialia*, 3 (4) (2007), pp. 607–610.
90. Ralph Spolenak, Stanislav Gorb, and Eduard Arzt, *Acta Biomaterialia*, 1 (1) (2005), pp. 5–13.
91. Christian Greiner, Ralph Spolenak, and Eduard Arzt, *Acta Biomaterialia*, 5 (2) (2009), pp. 597–606..
92. S.S. Brenner, *J. Applied Physics*, 27 (12) (1956), pp. 1484–1491.
93. S.S. Brenner, *J. Applied Physics*, 28 (9) (1957), pp. 1023–1026.
94. S.S. Brenner, *J. Applied Physics*, 30 (12) (1958), pp. 266–267.
95. P.M. Duxburry, *Statistical Models for the Fracture of Disordered Media* (St. Louis, MO: North-Holland Publishers, 1990), p. 189.
96. Michael D. Uchic et al., *Science*, 305 (5686) (2004), pp. 986–989.
97. Michael D. Uchic and Dennis M. Dimiduk, *Materials Science and Engineering A*, 400-401 (1-2 SUPPL) (2005), pp. 268–278.
98. Z.W. Shan et al., *Nat. Mater.*, 7 (2) (2008), pp. 115–119.
99. C.A. Volkert and E.T. Lilleodden, *Philosophical Magazine*, 86 (33) (2006), pp. 5567–5579.
100. C.P. Frick et al., *Materials Science and Engineering: A*, 489 (1-2) (2008), pp. 319–329.
101. J.R. Greer, W.C. Oliver, and W.D. Nix, *Acta Materialia,* 53 (6) (2005), pp. 1821–1830; "Erratum," *Acta Materialia*, 54 (6) (2006), p. 1705.
102. Julia R. Greer, Warren C. Oliver, and William D. Nix, *Acta Materialia*, 53 (6) (2005), pp. 1821–1830.
103. M. Zaiser et al., *Philosophical Magazine*, 8 (30) (2008), pp. 3861–3874.
104. Steffen Brinckmann, Ju-Young Kim, and Julia R. Greer, *Physical Review Letters*, 100 (15) (2008), p. 155502.
105. B.E. Schuster et al., *Acta Materialia*, 56 (18) (2008), pp. 5091–5100.
106. Z.W. Shan et al., *Physical Review B (Condensed Matter and Materials Physics)*, 77 (15) (2008), p. 155419.
107. C.A. Volkert, A. Donohue, and F. Spaepen, *J. Applied Physics*, 103 (8) (2008), p. 083539.
108. D.M. Dimiduk, M.D. Uchic, and T.A. Parthasarathy, *Acta Materialia*, 53 (15) (2005), pp. 4065–4077.
109. J.R. Greer and W.D. Nix, *Physical Review B (Condensed Matter and Materials Physics)*, 73 (24) (2006), p. 245410.
110. D. Kiener, W. Grosinger, and G. Dehm, *Scripta Materialia*, 60 (3) (2009), pp. 148–151.
111. D. Kiener et al., *Acta Materialia*, 56 (3) (2008), pp. 580–592.
112. H. Bei et al., *Scripta Materialia*, 57 (5) (2007), pp. 397–400.
113. H. Bei et al., *Applied Physics Letters*, 91 (11) (2007), p. 111915.
114. H. Bei et al., *Acta Materialia*, 56 (17) (2008), pp. 4762–4770.
115. K.S. Kumar, H. Van Swygenhoven, and S. Suresh, *Acta Materialia*, 51 (19) (2003), pp. 5743–5774.
116. M.W. Chen, E. Ma, and K.J. Hemker, *Nanomaterials Handbook,* ed. Yury Gogotsi (Boca Raton, FL: CRC Press, 2006), pp. 497–531.
117. D. Wolf et al., *Acta Materialia*, 53 (1) (2005), pp. 1–40.
118. M. Legros et al., *Philosophical Magazine A: Physics of Condensed Matter, Structure, Defects and Mechanical Properties*, 80 (4) (2000), pp. 1017–1026.
119. Zeljka Budrovic et al., *Science*, 304 (5668) (2004), pp. 273–276.
120. D. Pan et al., *Scripta Materialia*, 48 (12) (2003), pp. 1581–1586.
121. D.S. Gianola et al., *Scripta Materialia*, 55 (7) (2006), pp. 649–652.
122. D.S. Gianola et al., *Materials Science and Engineering: A*, 483-484 (2008), pp. 637–640.
123. G. Gottstein and L.S. Shvindlerman, *Grain Boundary Migration in Metals Thermodynamics, Kinetics, Applications* (Boca Raton, FL: CRC Press, 1999).
124. J.W. Cahn and J.E. Taylor, *Acta Materialia*, 52 (16) (2004), pp. 4887–4898.
125. J.W. Cahn, Y. Mishin, and A. Suzuki, *Acta Materialia*, 54 (19) (2006), pp. 4953–4975.
126. M. Ashby and D.R.H. Jones, *Engineering Materials 1: An Introduction to Properties, Applications and Design*, 3rd edition (St. Louis, MO: Butterworth-Heinemann, 2005).
127. D.T. Read, *International Journal of Fatigue*, 20 (3) (1998), pp. 203–209.
128. G.P. Zhang et al., *Microelectronics Reliability*, 47 (12) (2007), pp. 2007–2013.
129. Jun-Hyub Park, ManSik Myung, and Yun-Jae Kim, *Sensors and Actuators A: Physical*, 147 (2) (2008), pp. 561–569.
130. M.A. Eby, W.M. Sharpe, Jr., and G. Coles, *Proceedings Transducers '01* (Berlin: Springer-Verlag, 2001), pp. 1366–1369.

D.S. Gianola and C. Eberl are with Karlsruhe Institute of Technology, Karlsruhe, Germany and can be reached at Dan.Gianola@kit.edu, Chris.Eberl@kit.edu

Micro-Compression Testing of fcc Metals: A Selected Overview of Experiments and Simulations

Michael D. Uchic, Paul A. Shade, and Dennis M. Dimiduk

Micro-compression tests allow for the direct measurement of stress-strain behavior in volumes of material that have microscale dimensions. Initial studies worldwide have focused on the exploration of size-scale effects, where sample dimensions at the micrometer- and sub-micrometer scale can dramatically affect the fundamental processes of plastic deformation. Importantly, this scale of test volume can be directly modeled using state-of-the-art discrete dislocation simulations, the results of which have been essential to understanding the changes that can occur to dislocation mechanisms within small volumes. This combination of miniaturized testing and modeling that closely mimics these experiments provides a new pathway to characterize plastic flow on a highly localized basis.

INTRODUCTION

Uniaxial mechanical tests are perhaps the most commonly performed deformation experiments that provide basic design information. The popularity of these tests can be traced to the relative uniformity of the stress-state within the active region of the sample, which greatly aids in the subsequent interpretation of the test data. Tension tests are generally preferred because the stress-state in the gage section is more uniform compared to compression experiments, although compression experiments have selected advantages that include a simple and efficient sample shape, and a relatively uncomplicated procedure to place the sample within the loading train.

Shrinking uniaxial tension and compression test methods at the microscale provide a unique opportunity to study plastic deformation. One potential benefit is that the dimensions of the sample volume can be of similar size to the fundamental length scales for dislocation-based plastic flow. One can imagine that the processes of dislocation multiplication, annihilation, storage, glide, percolation, and so on, each has a characteristic length associated with that particular phenomenon.[1] When the sample dimensions approach these length scales, the proximity of the free surfaces potentially affect or alter these processes, which can result in observable changes in the material flow behavior.[1] Another potential advantage is that the finite sample volume can enable studies that probe the effect of local heterogeneities. For example, one can extract small samples from site-specific locations within a bulk crystal, where these samples might contain local changes in either chemistry or variations in microstructure (i.e., dislocation, grain, precipitate, void, defect, or other features), or both. Through testing of these isolated samples, one can more readily discern the influence that these internal variations have on mechanical properties, or help identify weak links within the microstructure. Another advantage of these microscale experiments is that they are amenable to study using sophisticated modeling methods such as three-dimensional (3-D) discrete dislocation simulations (DDS), where the entire test volume can be examined with ever-increasing fidelity. The 3-D DDS can calculate the stress-activated motion of all dislocations within the diminutive sample, allowing one to both visualize and quantify the dislocation activity that is responsible for plastic flow.

There are excellent examples of small-scale tension test methodologies in the literature that produce a well-understood and uniform stress state in samples with microscale dimen-sions.[2–5] However, these methods typically require samples produced by microelectronic processes (e.g., freestanding thin

How would you…

…describe the overall significance of this paper?

This paper provides a synopsis of some of the significant findings related to intrinsic size-scale strengthening effects and flow intermittency that have occurred in the past 4 years, which have been brought about either through the use of microcompression experiments, or subsequent modeling of these experiments using three-dimensional discrete dislocation simulations.

…describe this work to a materials science and engineering professional with no experience in your technical specialty?

The microcompression test is a relatively new experimental method that enables the measurement of uniaxial mechanical properties at the microscale. As mentioned above, this work provides a high-level overview of research that has examined microcompression experiments, focusing on studies that have discovered new size-dependent phenomena associated with plastic deformation, or that have provided a greater understanding of the mechanisms that are responsible for size-dependent mechanical behavior.

…describe this work to a layperson?

This paper summarizes new fundamental research that is focused on improving our understanding of the mechanisms that control the strength of materials. In particular, this paper describes experiments and simulations that examine how the physical dimensions of a structure affect the mechanisms that govern strength, especially when the scale of the structure is on the order of a few micrometers or smaller.

film samples that remain attached to a substrate). While this eases the difficulty in preparing small test volumes, these samples and corresponding microstructures are limited to materials and processing conditions available in microelectronic fabrication facilities. In order to circumvent this restriction, some of the present authors (along with Jeff Florando and William Nix) developed a micro-compression test methodology about six years ago.[6–9] In its present form, the methodology uses micromachining methods to produce compression samples within the surface of bulk materials, which are subsequently tested using a flat punch. The technique potentially allows one to explore deformation at small scales in a wide range of materials that can have complex chemistries, internal microstructures, and defect structures.

This article will highlight selected research that has utilized micro-compression testing or discrete dislocation modeling to examine the small-scale behavior of pure face-centered cubic (fcc) metals.

MICRO-COMPRESSION TEST METHOD

The micro-compression test methodology scales the conventional uniaxial compression experiment to the microscale using commercially available laboratory equipment.[6–9] A schematic of the test geometry is shown in Figure 1a, which highlights the relationship between the sample and a nanoindentation system that typically acts as the mechanical test frame. Other than the size-scale, the only significant difference between the conventional compression test and the micro-compression test is that there is no lower compression platen underneath the active gage section. Instead, the sample is integrally attached to the bulk substrate, and the transition region between the sample and substrate effectively acts as the lower platen. This sample geometry eliminates the need for micromanipulation equipment to place the sample within the test frame, which helps tremendously in the practical execution of the test. Also, the load and displacement rating and resolution of many commercial nanoindentation systems are ideal for performing micro-compression experiments.

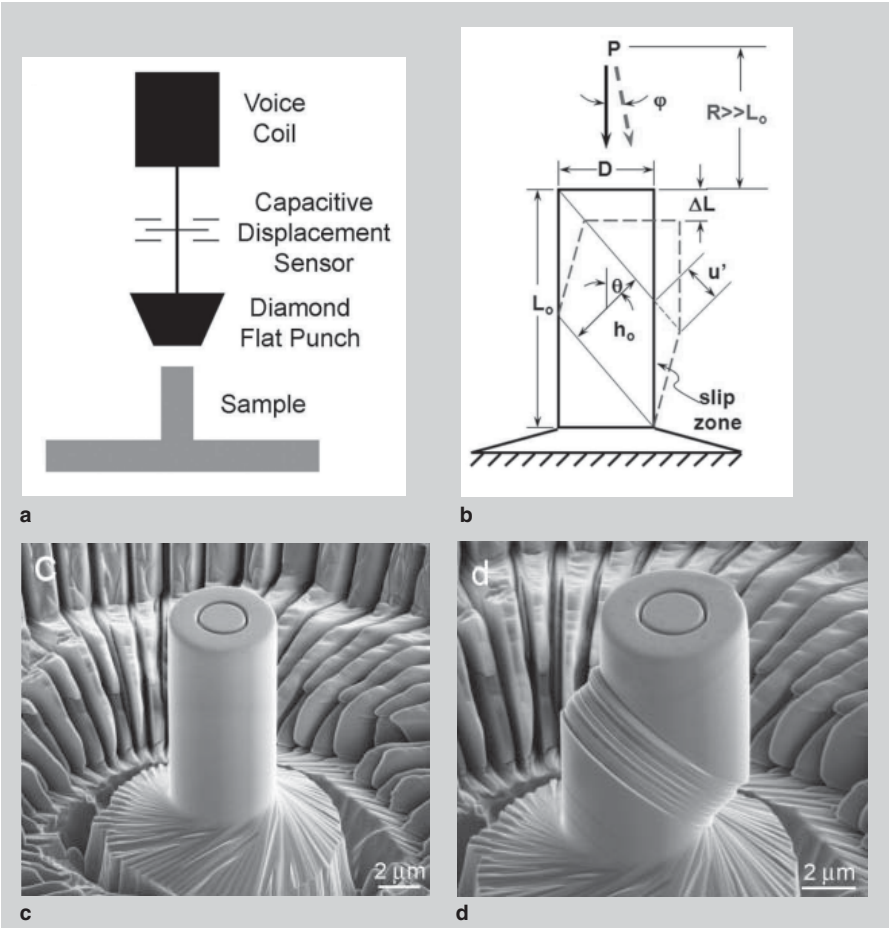

Figure 1. (a) A schematic of the microcompression test. (b) A schematic of the flow response of a microcrystal oriented for single slip. (c) A scanning electron image of a 5 μm diameter microcrystal sample of pure nickel oriented for single slip. (d) An SEM image of (c) after testing. The figure, taken from Reference 18, was originally adapted from Reference 9.

Micro-compression samples have been typically fabricated by focused ion beam (FIB) micromilling of bulk samples, [6–9] but alternative methods using larger-scale machining methods,[8] micro-electronic based[10] or other growth methods[11] have also been advanced to overcome limitations with FIB-based processing. Sample sizes have ranged from 0.25 μm to 80 μm in diameter, with corresponding gage lengths that varied from 1 μm to 160 μm. One significant advantage of FIB-prepared samples is they can be fabricated at very precise locations on a sample surface, such as within a single grain of a polycrystalline alloy, which potentially allows for measurement of single-crystal properties from polycrystalline materials. Disadvantages for FIB-prepared samples can include lengthy milling times and potential effects from the thin irradiation zone at the outer sample surface that remain a subject of current study.[10–15] An example of a FIB-micromachined and tested sample is shown in Figure 1c and 1d.[9]

Once fabricated, the samples are loaded into the nanoindentation frame, an individual sample is identified for testing, and the flat-punch tip is brought into contact with the top surface of the microsample in order to compress the sample volume. Prior to testing, the dimensions of the sample cross-sectional area and gage length are obtained, as these are needed to convert the load-displacement data into a stress-strain curve using the standard formulae for compression tests. These dimensions are usually determined from scanning electron microscope images. Examples of both load-controlled and displacement-controlled testing can be found in the literature, although most experiments have focused on performing constant displacement rate tests where the initial strain rate is approximately 10^{-3} to 10^{-4} s^{-1}.

EXPERIMENTAL RESULTS FOR fcc METALS

Figure 2 contains stress-strain data from representative micro-compression experiments conducted at room temperature on single-slip oriented pure nickel microcrystals that contain a moderate starting dislocation density ($\rho_o \sim 3\times10^{12}$ to 1×10^{13} m^{-2}).[7,9,16] From this figure, one can observe that the mechanical response of fcc microcrystals differs from bulk single-crystal behavior in the following ways. First, substantial strengthening is observed in microcrystals with decreasing sample volume, where this strengthening typically occurs at small-to-moderate plastic strains (< 5–10%). Second, the plastic flow response is intermittent and is composed of regions of easy glide with little to no strain hardening that are separated by regions of rapid hardening at elastic or nearly elastic rates. Third, the flow curves vary stochastically, and the variation in flow behavior intensifies with decreasing sample volume. All of these features are typical hallmarks of microcrystal flow.

Size-Dependent Strengthening

A closer inspection of Figure 2 shows that the increase in flow stress for microcrystals results from both an increase in the proportional limit, and enormous strain hardening rates at micro to moderate strains.[7,9,16] These enhanced strain-hardening rates are often greater than Stage II hardening (which is normally the highest strain hardening rate observed for bulk experiments on fcc crystals), and can approach a significant fraction of the elastic modulus.[9,16] This enhanced strain hardening behavior is size-scale dependent, with smaller samples exhibiting higher strain-hardening rates.[9,16,17] Taken to the extreme, pure-metal microcrystals with nanoscale dimensions can exhibit tremendous size-dependent strengthening. For example, the studies by C. P. Frick et al.[17] and Z.W. Shan et al.[15] report that 200 nm diameter, multiple-slip oriented pure nickel microcrystals can support stresses of 2 GPa and higher, in contrast to bulk yield stress values for single-crystal nickel that normally range from 10 MPa and higher.

One obvious question to ask is "What is the functional form between sample diameter and flow stress?" In the regime where size-dependent strengthening is observed, the relationship between the resolved shear stress (τ) and sample diameter (d) can be empirically described by a power law, which

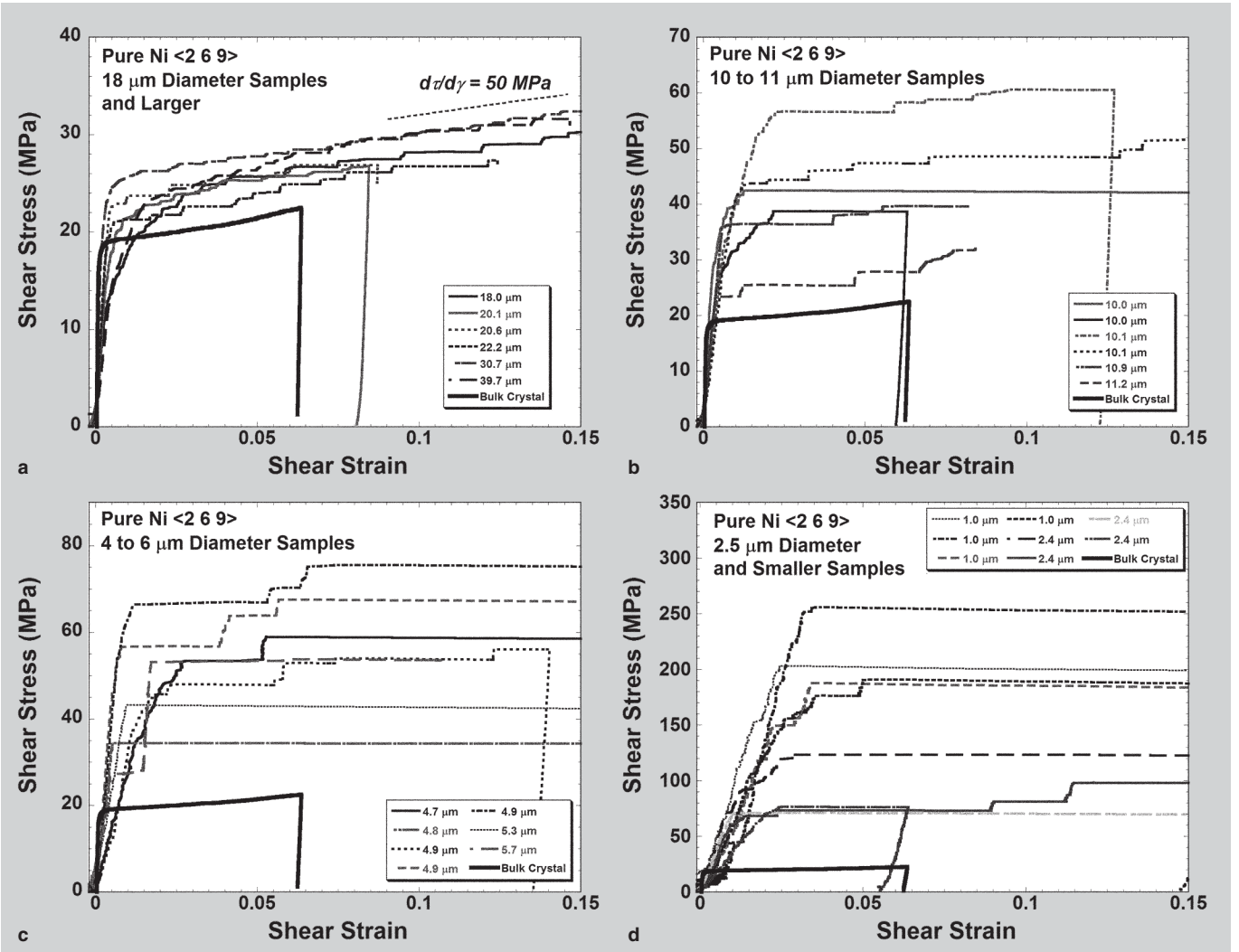

Figure 2. Shear stress-shear strain plots of <269>-oriented pure nickel microcrystals grouped by sample diameter: (a) 18 μm and larger, (b) 10–11 μm, (c) 4–6 μm, and (d) 2.5 μm and smaller. The thick black curve in each plot is from a macroscopic crystal of the same orientation, and plots are truncated at 15% strain for clarity. The figure is adapted from Reference 9.

is shown in Equation 1 in a form that normalizes the flow stress to provide a more accurate comparison of size-affected flow between different metals:

$$(\tau-\tau_o)\, b_{Ni} /(K_s\, b_{metal}) = Bd^{-n} \qquad (1)$$

where n is the power-law exponent, B is a constant, K_s is the anisotropic shear modulus, and b_{Ni}/b_{metal} is the relative ratio of the Burgers vector of each metal to a reference (selected to be nickel for the data shown in Figure 3). Figure 3 shows the normalized flow stress versus sample diameter for all of the pure-metal fcc size-dependent strengthening data from a number of different research studies.[18] By plotting the data in this way, one can see that all of this data collapses onto a single band, which generally holds for sample diameters that range from a couple hundred nanometers to tens of micrometers in diameter. A scaling exponent of 0.6 is a reasonable match to much of the data, assuming the reference stress, τ_o, is negligible. Note that the scaling exponent is different than those associated with grain-size strengthening (n = 0.5) or surface-controlled nucleation (n = 1).

Size-dependent strengthening is observed in both single-slip[7,9,19,20] and multiple-slip orientations.[10,17,21,22] Although no micro-compression study has examined the same material under both multiple- and single-slip orientations, the relative importance of crystal orientation lessens as the sample diameter shrinks to the micrometer scale, as the stress-strain curves for all orientations become qualitatively similar when size-affected behavior dominates plastic flow.

INTERMITTENCY AND STOCHASTIC FLOW

In addition to size-dependent strengthening, another almost-universally observed feature in fcc (and body-centered cubic [bcc]) microcrystals is an intermittency associated with plastic flow. By intermittency, we mean that microsamples, especially those that are single crystals, display a binary mechanical response composed of either periods of easy glide or elastic/nearly elastic loading. Intermittent flow is usually not observed in bulk materials save for well-known cases such as the Portevin-Le Chatelier effect, but these discrete bursts are regularly observed in microcrystal tests, and are clearly apparent in Figure 2.[9] Note that the curves shown in this figure are comprised of many hundreds or even thousands of discrete events that range from Angstroms to micrometers in scale,[23] although because of the construction of this figure only the largest events are observable. Micro-compression tests offer a unique means of studying this behavior, not only because the finite sample volume allows these events to be readily identified, but also because the test allows for the displacement associated with a strain burst to be directly measured[23] (unlike acoustic methods that measure the magnitude of a strain burst indirectly). In addition, one can also determine the stress,[20] time, and potentially the spatial location[24] associated with each event.

Although the strain bursts occur at stochastic intervals at stresses above the proportional limit, and the magnitude and timing of these events is also stochastic, the global statistics of strain bursts are well described by a power law. A quantitative analysis of these statistics has been performed by a number of independent studies.[20,23,25–28] These studies have correlated the frequency of occurrence of a given strain burst with its magnitude, and all agree that the number and magnitude of slip events display power-law scaling (with a cut off), in some cases spanning event sizes that range over three orders of magnitude. This power-law scaling is described by the following equation:[26]

$$n(x) = C\, x^{-\alpha} \exp[-(x/x_0)^2] \qquad (2)$$

where n(x) is the probability of an event of magnitude x, C is a constant, α is the power law scaling exponent, and x_0 is the characteristic magnitude of the largest strain burst. The value of α is reported to be approximately 1.6 for much of the experimental data published to date,[20,23,25–28] but one study showed that this value is dependent upon the applied strain rate.[25] Some studies have sought to further quantify the relationship between slip events by examining other correlation statistics.[20] Although these types of experimental studies are relatively new, the discovery of this behavior has current practical implications on plastic forming at the microscale[26] and long-term implications on the development of new meso-scale deformation theories.[23]

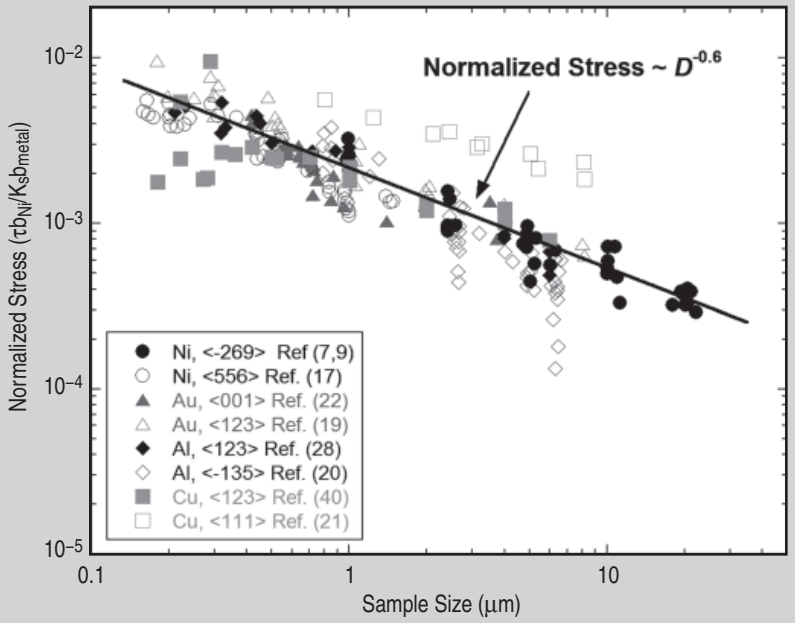

Figure 3. A composite plot of published microcrystal flow stress data as a function of sample diameter for fcc metals. The scaling exponent *n* that best fits the data is approximately 0.6. The figure is adapted from Reference 18.

3-D DISCRETE DISLOCATION SIMULATIONS

As mentioned in the introduction, the diminutive size of microcrystals en-

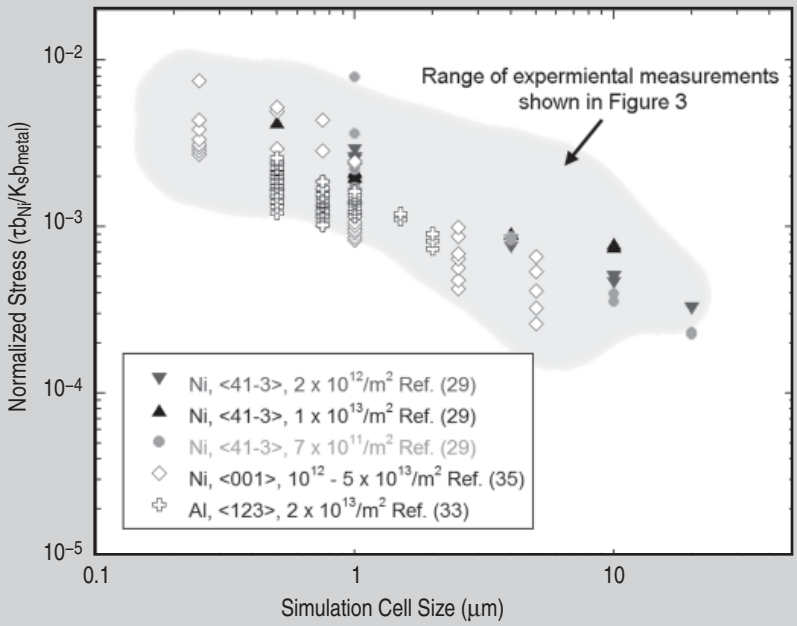

Figure 4. A composite plot of published flow-stress data for 3-D DDS as a function of simulation cell size. Data in the plot have been normalized by the shear modulus and Burger's vector used for each study (see Equation 1). The shaded area designates the range of experimental measurements shown in Figure 3. The figure is adapted from Reference 18.

ables the use of 3-D DDS to model the entire sample volume.[26,29–36] This simulation method is well suited to study the problem of microcrystal flow, as it can naturally account for both the far-field and local interactions between dislocations, as well as accurately track the motion of dislocations, including those that are in contact with the nearby free surfaces. It is important to note that at present these methods at best mimic the microcrystal experiments, and also vary considerably in some critical areas. One particularly crucial issue pertains to the initial dislocation substructure, especially with regards to the number, size, and distribution of dislocation sources. All of the published studies contain moderate-to-high dislocation densities that are similar or greater than those found in the microcrystal experiments, and most of these studies instantiate the initial dislocation density as a set of Frank–Read sources (FRS) having rigidly fixed ends.[26,29–35] However, the strength and distribution of the initial FRS can vary significantly from study to study, which can strongly affect the outcome of the simulations.[18] Other differences include the following: whether cross slip is allowed, whether the influences of the free surfaces and the test boundary conditions are included, the magnitude of the applied strain rate, the loading mode, crystal orientation, sample aspect ratio, and the size of the simulation volume. In spite of these differences, the results from state-of-art 3-D DDS have made a significant impact on the understanding of microcrystal deformation.

Importantly, many of these simulations display size-dependent strengthening, enhanced strain-hardening rates at small strains, and intermittent flow, which are all consistent with the aforementioned hallmarks of microcrystal flow.[26,29–36] As an example, Figure 4 plots the size-dependent strengthening observed in the 3-D DDS studies, the majority of which fall within the range of data that was determined from experiments.[18] With regards to the mechanisms that are responsible for this behavior, this article highlights two new mechanisms[29,30] that are observed in many of the simulations.

The first new mechanism provides an increase in the strength of existing dislocation sources due to the proximity of free surfaces—a process termed source-truncation hardening.[29,30] Source truncation occurs during the initial operation of an FRS, where the interaction of a single FRS source with the nearby free surfaces separates the FRS into two single-arm sources. Depending on the sample size, these single-arm sources may have minimum arm lengths that are much smaller than the original FRS length, and thus each of these single-arm sources would require a significantly higher stress to operate than the original source. In selected simulations, spiraling single-arm sources have been observed to account for almost all of the plastic strain,[29,34–36] and thus the flow stress is controlled by the largest single-arm sources and their respective Schmid factors.[29] A statistical analysis of the source-truncation mechanism has shown that this process can account for much of the size-dependent strengthening observed experimentally.[37]

The other new size-dependent mechanism identified by three independent studies[29,33,36] is related to the paucity of dislocation sources in microcrystals. Unlike bulk crystals that have an almost infinite supply of potential sources, microcrystals have only a finite number of available sources, and one can imagine that the plastic flow of microcrystals is therefore more sensitive to the termination of an active source due to typical forest-hardening processes. If this happens, the stress increment required to activate the next-weakest source may be much larger than would be required in a bulk crystal, simply because of the limited number of possible sources that the sample has to choose from. The reduced number of weak links in the dislocation microstructure can result in much more potent average strain-hardening rates, especially in the small-strain regime. Consequently, the flow behavior in many fcc microcrystals takes place intermittently via the sequential activation and obstruction of the weakest sources, and this process is termed exhaustion hardening.[9,29] By this mechanism, a micrometer-scale crystal may be starved of mobile dislocation density, even at sizes where the effects of image forces and free surfaces are dramatically reduced. This mechanism of enhanced forest hardening is believed to be responsible for the strengthening effects extending to microcrystal sizes exceeding 20 micrometers in diameter.[29]

The combination of source-truncation and exhaustion hardening convincingly accounts for the observation

of stochastic flow in 3-D DDS. For the same starting density, different instantiations of the initial dislocation substructure result in changes to both the distribution of largest single-arm source lengths, as well as the probability that a dislocation reaction will terminate operation of these largest sources. It naturally follows that the resultant flow curves will vary randomly with these local rearrangements. At a fixed density, the stochastic response becomes more pronounced as the simulation cell size decreases, as there are potentially fewer sources that can operate at nearly the same stress, thereby maximizing the influence of any individual source. Also, the magnitude of the size-affected response is directly dependent on the initial density, as higher starting densities result in a weaker scaling response (more available sources) and vice-versa.[29] This dependence results in behavior that is counter to classical strengthening ideas, i.e., an increase in the initial density can soften microcrystals,[29] which has been confirmed experimentally.[38]

CONCLUSIONS

The micro-compression experiments and simulations described have made a significant impact on the study of dislocation-based deformation processes. These studies have clearly demonstrated that size-scale effects exist independently of other previously known size effects such as nucleation-controlled deformation or the presence of imposed strain gradients. Notably, the close coupling of experiments and simulations has led to the discovery of new strengthening mechanisms that are active in microscale samples. The small sample volumes also facilitate the measurement of stochastic dislocation activity (strain bursts), which has greatly aided the understanding of how dislocation ensembles dissipate energy, and hopefully will help advance new meso-scale deformation theories.

With continued effort, we predict that this type of experimental methodology will allow one to locally determine the full suite of properties of various microconstituents (phases, precipitates) in fully processed engineering materials. Challenges in the area of sample fabrication and testing include developing parallelized fabrication methods that can be applied to a wide range of materials, and in performing a broader suite of testing modes (tension[39] and elevated temperature testing, for example). Similar areas of improvement exist for the modeling and simulation tools, such as incorporating realistic starting dislocation networks or internal microstructures, as well as simulating larger volumes that truly bridge the gap between micro- and meso-scopic deformation.

ACKNOWLEDGEMENTS

The authors have been supported by the Air Force Research Laboratory, Air Force Office of Scientific Research, and the Defense Advanced Research Projects Agency. PAS also acknowledges support from the AFRL/RX Science and Technology for the 21st Century Program. The authors also thank Triplicane Parthasarathy, Satish Rao, and Chris Woodward for their contributions toward preparing this manuscript.

References

1. J. Gil Sevillano, I. Ocana Arizcorreta, and L.P. Kubin, *Mater. Sci. Eng. A*, 309-310 (2001), pp. 393–405.
2. M.A. Haque and M.T.A. Saif, *Scripta Materialia,* 47 (2002), pp. 863–867.
3. H.D. Espinosa, B.C. Prorok, and M. Fischer, *J. Mech. Phys. Solids,* 51 (2003), pp. 47–67.
4. Y. Zhu and H.D. Espinosa, *PNAS,* 102 (2005), pp. 14503–14508.
5. D.Y.W. Yu and F. Spaepen, *J. Appl. Phys.*, 95 (2004), pp. 2991–2997.
6. M.D. Uchic et al., *Mater. Res. Soc. Symp. Proc.*, 753 (2003), pp. BB1.4.1–1.4.6.
7. M.D. Uchic et al., *Science,* 305 (2004), pp. 986–989.
8. M.D. Uchic and D.M. Dimiduk, *Mater. Sci. Eng. A,* 400-401 (2005), pp. 268–278.
9. D.M. Dimiduk, M.D. Uchic, and T.A. Parthasarathy, *Acta Materialia,* 53 (2005), pp. 4065–4077.
10. J.R. Greer and W.D. Nix, *Phys. Rev. B,* 73 (2006), p. 245410.
11. H. Bei et al., *Scripta Materialia,* 57 (2007), pp. 397–400.
12. D. Kiener et al., *Mater. Sci. Eng. A,* 459 (2007), pp. 262–272.
13. C. Motz, T. Schoberl, and R. Pippan, *Acta Materialia,* 53 (2005), pp. 4269–4279.
14. H. Bei et al., *Appl. Phys. Lett.,* 91 (2007), p. 111915.
15. Z.W. Shan et al., *Nature Materials,* 7 (2008), pp. 115–119.
16. D.M. Norfleet et al., *Acta Materialia,* 56 (2008), pp. 2988–3001.
17. C.P. Frick et al., *Mater. Sci. Eng. A,* 489 (2008), pp. 319–329.
18. M.D. Uchic, P.A. Shade, and D.M. Dimiduk, "Plasticity of Micrometer-Scale Single Crystals in Compression: A Critical Review," submitted for publication to *Annual Reviews of Materials Research.*
19. C.A. Volkert and E.T. Lilleodden, "Size Effects in the Deformation of Sub-Micron Au Columns," *Phil. Mag.,* 86 (2006), pp. 5567–5579.
20. K.S. Ng and A.H.W. Ngan, *Acta Materialia*, 56 (2008), pp. 1712–1720.
21. D. Kiener et al., *Adv. Eng. Mater.,* 8 (2006), pp. 1119–1125.
22. J.R. Greer, W.C. Oliver, and W.D. Nix, *Acta Materialia,* 53 (2005), pp.1821–1830; Erratum, *Acta Materialia,* 54 (2006), p. 1705.
23. D.M. Dimiduk et al., *Science,* 312 (2006), pp. 1188–1190.
24. M.D. Uchic et al., *Scripta Materialia,* 54 (2006), pp. 759–764.
25. D.M. Dimiduk et al., *Modelling Simul. Mater. Sci. Eng.*, 15 (2007), pp. 135–146.
26. F.F. Csikor et al., *Science,* 318 (2007), pp. 251–254.
27. M. Zaiser et al., "Strain Bursts in Plastically Deforming Molybdenum Micro- and Nanopillars," *arXiv.org* (Ithaca, NY: Cornell Unviersity, 2008), arXiv:0802.1843v1.
28. S. Brinckmann, J.Y. Kim, and J.R. Greer, *Phys. Rev. Lett.,* 100 (2008), p. 155502.
29. S.I. Rao et al., *Acta Mater.,* 56 (2008), pp. 3245–3259.
30. S.I. Rao et al., *Phil. Mag.,* 87 (2007), pp. 4777–4794.
31. H. Tang, K.W. Schwarz, and H.D. Espinosa, *Acta Materialia,* 55 (2007), pp. 1607–1616.
32. D. Weygand et al., *Mater. Sci. Eng. A,* 483 (2008), pp. 188–190.
33. J. Senger et al., *Scripta Materialia,* 58 (2008), pp. 587–590.
34. J. El-Awady, S.B. Biner, and N.M. Ghoniem, *J. Mech. Phys. Solids,* 56 (2008), pp. 2019–2035.
35. J. El-Awady, M. Wen, and N.M. Ghoniem, "The Role of the Weakest-Link Mechanism in Controlling the Plasticity of Micropillars," (2008), submitted for publication.
36. H. Tang, K.W. Schwarz, and H.D. Espinosa, *Phys. Rev. Lett.*, 100 (2008), p. 185503.
37. T.A. Parthasarathy et al., *Scripta Materialia,* 56 (2007), pp. 313–316.
38. H. Bei et al., *Acta Materialia,* 56 (2008), pp. 4762–4770.
39. D. Kiener et al., *Acta Materialia,* 56 (2008), pp. 580–592.
40. O. Kraft and C.A. Volkert, "Size Effects on Deformation and Fatigue of Thin Films and Small Structures" (Paper presented at CAMTEC, Cambridge University, 2006).

Michael D. Uchic and Dennis M. Dimiduk are with Air Force Research Laboratory, Materials & Manufacturing Directorate, Wright-Patterson AFB, OH 45433; Paul A. Shade is with The Ohio State University, Department of Materials Science and Engineering, Columbus, OH. Dr. Uchic can be reached at michael.uchic@wpafb.af.mil.